Wideband Waveforming for Integrated Data and Energy Transfer: Creating Extra Gain Beyond Multiple Antennas and Multiple Carriers

Zhonglun Wang, *Student Member, IEEE,* Jie Hu, *Senior Member, IEEE,* Kun Yang, *Fellow, IEEE* and Kai-Kit Wong, *Fellow, IEEE*

***Abstract*—When wideband signals propagate in a rich-scatterer environment, we obtain abundant resolvable multiple transmission paths to form a number of virtual antennas. Therefore, substantial spatial gain can be attained by carefully waveforming in all these resolvable transmission paths without additional antennas. This resultant spatial gain is then exploited for improving the performance of integrated-data-and-energy-transfer (IDET) from a single transmitter to multiple receivers. We aim to maximise the downlink fair-throughput and sum-throughput, while satisfying the energy harvesting requirements by jointly optimising the waveformers at the transmitter and the power splitters at the receivers. A low-complexity fractional-programming (FP) based alternating algorithm is proposed to solve these non-convex optimisation problems. The non-convex wireless energy transfer (WET) constraints are transformed to be convex with a modified quadratic transform (MQT) method. As a result, the stationary points for both the fair-throughput and the sum-throughput maximisation problems are obtained. The numerical results demonstrate the advantage of our proposed algorithm over a minimum-mean-square-error (MMSE) scheme, a zero-forcing (ZF) scheme and a time-reversal (TR) scheme. Simulation results show that the wireless data transfer (WDT) performance of our scheme outperforms the single-input-single-output orthogonal-frequency-division-multiple-access (SISO-OFDMA) when the output direct current (DC) power requirement is high. When we have a practical individual subcarrier power constraint, the WDT performance of our scheme outperforms multiple-input-single-output orthogonal-frequency-division-multiplex-access (MISO-OFDMA).**

***Index Terms*—Wideband communication, wideband waveformer, integrated data and energy transfer (IDET), fractional programming (FP).**

This paper was partly funded by Natural Science Foundation of China (No. 62132004, 61971102), MOST Major Research and Development Project (No. 2021YFB2900204), Sichuan Science and Technology Program (No. 2022YFH0022 and 22QYCX0168), UESTC Yangtze Delta Region Research Institute-Quzhou (No. 2022D031), and EU H2020 Project COSAFE (GA-824019).

Zhonglun Wang and Jie Hu are with the School of Information and Communication Engineering, University of Electronic Science and Technology of China, Chengdu 611731, China (e-mail: 202021010524@std.uestc.edu.cn; hujie@uestc.edu.cn).

Kun Yang is with the school of Information and Communication Engineering, University of Electronic Science and Technology of China, Chengdu, 611731, China and also with the School of Computer Science and Electronic Engineering, University of Essex, Colchester, CO4 3SQ, U.K. (e-mail: kunyang@essex.ac.uk).

Kai-Kit Wong is with the Department of Electronic and Electrical Engineering, University College London, WC1E 6BT London, U.K. (e-mail: kai-kit.wong@ucl.ac.uk).

I. Introduction

In the 6G era, the number of the Internet of Things (IoT) devices is growing explosively and exceeding 10^7 devices/km^2 [1]. Sufficient energy supply is crucial to guarantee that IoT networks operate efficiently. In order to avoid replacing batteries frequently, IoT networks should be self-sustainable by exploiting wireless energy transfer (WET) technologies [2]. Therefore, considering WET as a new service class with conventional wireless data transfer (WDT) yields integrated data and energy transfer (IDET), which is recognized as one of the potential technologies towards "zero-energy" IoT networks in 6G [3]–[5].

In order to improve its efficiency, coding and modulation were relied upon for generating proper IDET waveforms. Specifically, Zhao *et al.* [6] characterised the generation of coherent binary codes and modulation symbols by exploiting Markov chains, and obtained the optimal codebook to maximise WET performance with mutual information constraints. Zhang *et al.* [7] then investigated the transmit spatial modulation (TSM) with the IDET. One receive antenna was used for WDT with TSM, while the remainder receive antennas were used for WET. Furthermore, Zhao *et al.* [8] investigated IDET by utilizing receive spatial modulation (RSM). RSM is capable of achieving low-hardware complexity since the receiver antenna can obtain the index information directly. Moreover, time index modulation and frequency index modulation based IDET networks were investigated in [9]–[11]. As one of the most classic waveforms, orthogonal frequency division multiplexing (OFDM) is widely applied in IDET. Yin *et al.* [12] investigated IDET by exploiting OFDM and power splitting. Moreover, in [13]–[15], Clerckx *et al.* superimposed stochastic information symbols and deterministic energy symbols in the same OFDM subcarrier. As the deterministic energy symbols were known by the receiver, their adverse impact on the WDT performance could be cancelled. As a result, the WET performance was substantially improved without sacrificing the WDT performance.

Moreover, the IDET waveform was also studied in the spatial domain by invoking the multiple-input multiple-output (MIMO) technique. Zhang *et al.* [16] investigated the rate-energy region of IDET in the MIMO broadcast channel. Increasing the number of antennas increased the spatial gains, which substantially improved the IDET performance [17]. Intelligent reflecting surface (IRS) is capable of generating

reflection paths between the transmitter and the receivers, which also substantially improves the IDET efficiency [18]–[20]. Moreover, Yue *et al.* [21] considered several practical waveforms in the IRS-assisted IDET. They demonstrated that the WET performance of deterministic waveforms outperformed the Gaussian counterparts.

The current narrowband IoT (NB-IoT) can satisfy low throughput, low device density and simple application scenarios. However, in the 6G era, the wideband IoT may be extensively utilized to provide the services that the NB-IoT cannot provide. Wideband IoT can provide a higher data rate, which is suitable for high-definition video streaming, remote monitoring and real-time data analytics. Moreover, compared to NB-IoT, wideband IoT can support more large-scale connections (although the access density is lower than the NB-IoT) through the single-carrier time-reversal division multiple access [22] and multi-carrier orthogonal frequency-division multiple access (OFDMA) [23] technologies, which may be used in smart industry, smart cities and logistics management.

With a nanosecond time resolution, wideband signals are capable of distinguishing diverse transmission paths in rich scattering environments, this is the spatial diversity of the wideband channel [24]. Multi-carrier transmission (MCT) techniques are well known to overcome multipath fading. MCT divides wideband into many narrow bands to overcome frequency-selective fading by techniques, such as the classic OFDM. Moreover, different from OFDM, single-carrier receivers with a wideband waveformer were capable of directly decoding information without the channel state information (CSI) [1] [25]. Due to its low complexity, the single-carrier architecture is more suitable for low power sensors. Carefully designing the waveforms in every resolvable transmission path may effectively adjust the amplitude and phase of the information symbols, the inter-symbol-interference (ISI) symbols and the inter-receiver-interference (IRI) symbols, which results in more abundant spatial gain. Therefore, a number of wideband waveforms were investigated for WDT and WET.

The time-reversal (TR) generated a resonance effect in the time domain, which might effectively decrease the ISI and IRI [26]. In [27]–[29], the TR waveform was leveraged for WDT. Similarly, Daniels *et al.* [30] proposed a zero-forcing (ZF) waveform to overcome the multipath effect. Moreover, Yang *et al.* [31] designed an optimal minimum mean square error (MMSE) waveform when cancelling the ISI in the TR system. In order to explore the WET potential, the power waveforms were proposed to leverage the spatial gain. Ku *et al.* [32] proposed a single-tone waveform, which was capable of achieving high WET performance. Furthermore, they designed deterministic periodic signals by exploiting the eigenvalue decomposition method and obtained the optimal wideband WET performance [33].

[1]In line with [25], after waveforming at the transmitter and transmitting through the multipath channel (equivalent to do equalization operation on the air), the phase-offset of the information symbols is eliminated. The IDET receivers decode information symbols by onetap detection and do not require equalization, which indicates that we do not need the CSI in the IDET receivers.

The IDET system may benefit from single-carrier wideband waveforming, which is discussed as follows:

- Compared to the traditional narrowband waveform, the single-carrier wideband waveform can achieve a 6 dB gain in WET performance by exploiting the spatial gain [32], which leads to higher energy efficiency.
- Traditional OFDM-based IDET system assumes that the subcarriers are orthogonal to each other and are designed in the frequency domain. The single-carrier wideband IDET waveform is designed in the time domain. At the OFDM receivers, FFT and equalization operations are required [34], which results in higher hardware complexity and power consumption. The single-carrier wideband receivers decode information symbols by adopting onetap detection [25], which has lower hardware and computational complexity. Compared to the OFDM waveform, the single-carrier wideband waveform has a lower peak-to-average-power ratio (PAPR) [22]. Therefore, the single carrier wideband waveform is more suitable for the IDET receivers which require a simpler circuit.
- Rather than separately designing the WET and WDT waveforms with different goals, optimally designing the IDET waveform may achieve a balance between the WET and WDT performance by exploiting the full-potential of the additional spatial gain.

Therefore, the single carrier wideband waveform is suitable for the IDET system, where high data throughput, high WET performance and low complexity can be achieved simultaneously.

Most of the existing works designed the IDET system by adopting beamforming techniques with narrowband signal or OFDM. The narrowband signal with lower time resolution cannot utilize the spatial gain caused by the resolvable paths to improve the IDET performance. The OFDM-based IDET system utilizes frequency diversity in the frequency domain. However, existing works did not design the IDET waveform in the time domain and obtain the full-potential of the spatial gain incurred by the resolvable transmission paths to design the IDET towards the multiple receivers. Against this background, our contributions are summarized as follows:

- A single carrier wideband-based IDET system with a single transmitter and multiple receivers is investigated. We adopt the power splitting scheme for simultaneously receiving data and energy. Optimal waveforms are designed for maximising the fair-throughput and the sum-throughput, respectively.
- A modified quadratic transform (MQT) method is proposed to avoid the high complexity semi-definite relaxation (SDR). We convert the non-convex objective function and constraints into convex ones by adopting fractional programming (FP), with a quadratic transform (QT) method and a MQT method. Finally, we alternatively optimise the waveformers and the power splitters for obtaining the optimal IDET performance.
- The simulation results verify that our proposed optimal scheme outperforms the existing waveforms, such as TR, ZF and MMSE. Moreover, the WET performance gains

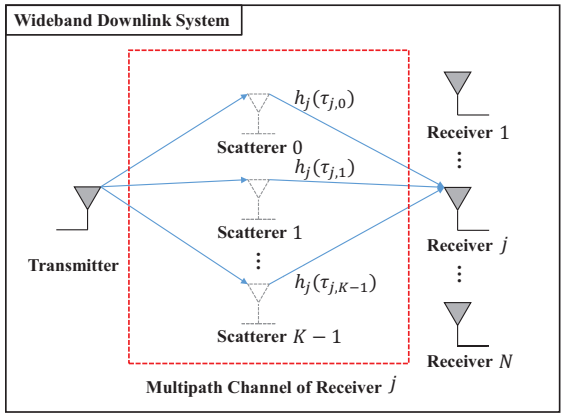

Fig. 1. Wideband channel model.

of our proposed schemes are better than the single-input single-output OFDMA (SISO-OFDMA). When we have a practical individual subcarrier power constraint, the WDT performance of our scheme outperforms multiple-input-single-output OFDMA (MISO-OFDMA).

Notations: For vectors $\mathbf{x}$ and $\mathbf{y}$, $\mathbf{x}^T$ refers to its transpose, $\|\mathbf{x}\|_2$ refers to its Euclidean norm, and $\mathbf{x} * \mathbf{y}$ refers to the linear convolution operation of the two vectors. For a matrix $\mathbf{X}$, $\mathbf{X}^\dagger$ refers to the conjugate transpose. $\mathbb{N}$ denotes the set of nonnegative integers. $\mathbb{R}$ denotes the set of real numbers. $\mathbb{C}$ denotes the set of complex numbers. $\mathbb{S}_{++}$ denotes the set of positive definite matrixs. Moreover, $\lfloor\cdot\rfloor$ denotes the floor operation, $\mathbb{E}[\cdot]$ refers to the expection operation and $\mathcal{R}\{\cdot\}$ denotes the real part. The operator $[x]^+ = \max(x, 0)$, for $\forall x \in \mathbb{R}$.

II. System Model

A. Wideband Channel

As portrayed in Fig. 1, we have abundant scatterers distributed in wireless environments. Wideband signals are assumed to be only scattered once by a single scatterer in a transmission path from the IDET transmitter to the receivers. We have a single IDET transmitter and N receivers in the system. With K scatterers distributed in the environment, the continuous multipath channel impulse response of the j-th receiver is defined as

$$h_j(t) = \sum_{k=0}^{K-1} \alpha_{j,k} \delta\left(t - \tau_{j,k}\right), \quad j = 1, 2, \cdots, N, \tag{1}$$

where $\alpha_{j,k}$ is the multipath coefficient of the k-th scatterer and $\tau_{j,k}$ is the corresponding transmission delay. The function $\delta(\cdot)$ denotes the unity impulse with $\delta(t) = 0$ for $t \neq 0$ and $\int_{-\infty}^{\infty} \delta(t)dt = 1$. The bandwidth of the transmit signal is denoted as B and the corresponding coherent time is $T_s = 1/B$. Specifically, the channel coefficient $h_j[l]$ in the l-th transmission path is expressed as

$$h_j[l] = \int_{\tau_{j,0}+lT_s}^{\tau_{j,0}+(l+1)T_s} W\left(\tau_{j,0} + lT_s - t\right) h_j(t)dt, \tag{2}$$

where $\tau_{j,0}$ represents the lowest propagation delay among multiple transmission paths towards the j-th receiver and $W(\cdot)$ is a window function with a length of T_s. The equivalent channel coefficient of the l-th resolvable transmission path for the j-th receiver is expressed as $h_j[l] = \sqrt{\Omega_j} v_{j,l}$. The circular symmetric complex Gaussian (CSGC) random variable $v_{j,l}$ is the small-scale fading in the l-th resolvable path with a zero mean and a variance of

$$\mathbb{E}\left[\left|v_{j,l}\right|^2\right] = \exp\left(-lT_s / \widetilde{\tau}_{rms,j}\right), \tag{3}$$

where $\widetilde{\tau}_{rms,j}$ is the root-mean-square (RMS) delay spread of the j-th receiver [35]. We define $\tilde{\boldsymbol{\tau}}_{rms} = [\widetilde{\tau}_{rms,1}, \cdots, \widetilde{\tau}_{rms,N}]$. The path-loss of the j-th receiver is expressed as

$$\Omega_j = \Omega_0 d_j^{-\beta}, \tag{4}$$

where $\Omega_0 = G_t G_r (c/4\pi f_c)^2$ is the pass-loss at the reference distance 1 m, G_t and G_r are the transmit and receive antenna gains, respectively [36]. Moreover, in the path-loss model, c is the speed of light, f_c is the carrier frequency and β is the path-loss exponent, while d_j is the distance between the transmitter and the j-th receiver. The delay spread of the j-th receiver is then expressed as $\widehat{\tau}_j = \max_k \left\{\tau_{j,k} - \tau_{j,0}\right\}$. The maximum number of the resolvable transmission paths between the IDET transmitter and the j-th receivers is $L_j = \left\lfloor \widehat{\tau}_j B \right\rfloor$. By denoting $L = \max_j L_j$, the multipath channel coefficient vector of the j-th receiver can be denoted as [2]

$$\mathbf{h}_j = \left[h_j[0], h_j[1], \cdots, h_j[L-1]\right]^T, \tag{5}$$

where $h_j[l] = 0$ for $l \geq L_j$.

B. Transmitter Architecture

As portrayed in Fig. 2, the transmitter performs a series of processing on the original modulated symbols for the N receivers. The modulated symbol stream requested by the j-th receiver is denoted as $\mathbf{s}_j = \left[s_j[0], s_j[1], \cdots, s_j[M-1]\right]$, where the symbol $s_j[m]$ is a complex Gaussian random variable with a zero mean and unity variance. In order to adjust the modulated symbol rate to the sampling rate [39], we up-sample the original symbol sequence $\mathbf{s}_j$ with a factor $\mathcal{D}$, which results in a new symbol sequence $\mathbf{s}_j^{\mathcal{D}} = \left[s_j^{\mathcal{D}}[0], s_j^{\mathcal{D}}[1], \cdots, s_j^{\mathcal{D}}[M\mathcal{D}-1]\right]$ with a length of $M\mathcal{D}$. This new symbol sequence is defined as

$$s_j^{\mathcal{D}}[m] = \begin{cases} s_j[m/\mathcal{D}], & \mathrm{mod}(m, \mathcal{D}) = 0, \\ 0, & \text{otherwise}, \end{cases} \tag{6}$$

for $\forall j = 1, 2, \cdots, N$. As shown in Fig. 2, after the rate adjustment, the resultant symbol sequence $\mathbf{s}_j^{\mathcal{D}}$ is then processed by a waveformer $\mathbf{g}_j = \left[g_j[0], g_j[1], \cdots, g_j[L-1]\right]^T$ [3].

[2]Prior to the downlink transmission, the IDET receiver transmits a pseudo random sequence to the transmitter, which the CSI is estimated. After processing by the Golay correlator in the transmitter, the CSI quality is boosted quickly [37]. In addition, the CSI is quiet in the indoor environment, which indicates the channel need not to be estimated frequently [38].

[3]The waveformer is different from the pulse shape filter. The waveformer is used to adjust the amplitude and phase of each IDET symbol, which is capable of balancing the WDT and WPT performance. The pulse shape filter is used to limit the effective bandwidth of the IDET system [40].

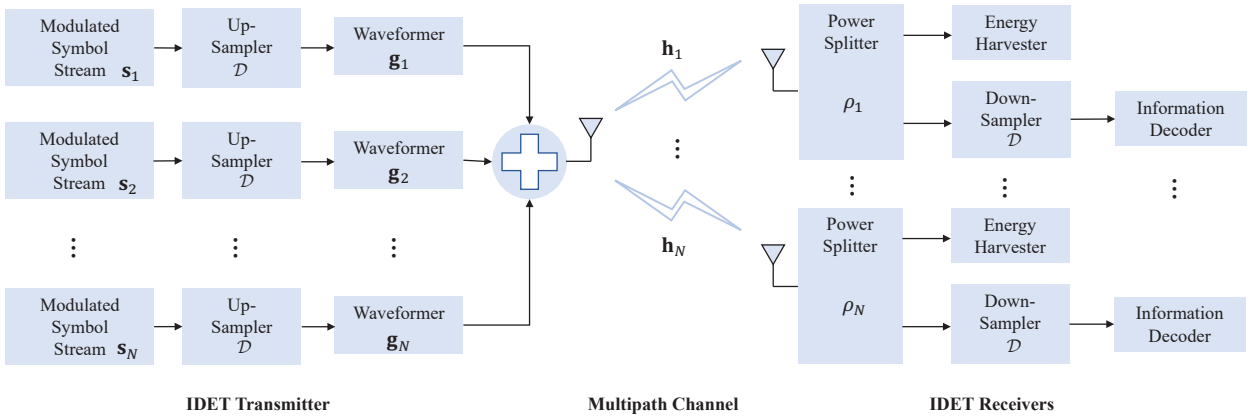

Fig. 2. Multi-receiver system model.

Theorem 1: When the maximum transmit power at the transmit antenna is P_{tx}, the total power of the waveformer satisfies $\sum_{j=1}^{N} \left\|\mathbf{g}_j\right\|_2^2 = \mathcal{D}P_{tx}$.

Proof 1: Proved in Appendix A.

Finally, all the signals are combined and transmitted via the wideband channel.

C. Receiver Architecture

When the wideband signal arrives at the j-th IDET receiver, the m-th received symbol can be expressed as

$$y_j^{\mathcal{D}}[m] = \sum_{n=1}^{N} \left(\mathbf{s}_n^{\mathcal{D}} * \mathbf{g}_n * \mathbf{h}_j\right)[m] + z_j^{\mathcal{D}}[m], \tag{7}$$

where $z_j^{\mathcal{D}}[m]$ is the additive complex Gaussian noise gleaned by the antenna with a zero mean and a variance of σ_z^2. Then the signal is split into two portions by the power splitter for information decoding and energy harvesting. A portion of the m-th symbol $y_{EH,j}^{\mathcal{D}}[m]$ received by the j-th receiver for energy harvesting is expressed as

$$\begin{aligned} y_{EH,j}^{\mathcal{D}}[m] &= \sqrt{\rho_j} \sum_{n=1}^{N} \left(\mathbf{s}_n^{\mathcal{D}} * \mathbf{g}_n * \mathbf{h}_j\right)[m] + \sqrt{\rho_j} z_j^{\mathcal{D}}[m] \\ &= \sqrt{\rho_j} \sum_{k=1}^{2L-1} \sum_{n=1}^{N} \mathbf{H}_j^{(k)} \mathbf{g}_n s_n^{\mathcal{D}}[m-k+1] + \sqrt{\rho_j} z_j^{\mathcal{D}}[m], \end{aligned} \tag{8}$$

where ρ_j is the power splitting ratio of the j-th receiver. The matrix $\mathbf{H}_j \in \mathbb{C}^{(2L-1)\times L}$ is the Toeplitz matrix with the vector $\left[\mathbf{h}_j^T, \mathbf{0}^T\right]^T$ as its first column. It is invoked for equivalently transforming the convolution between a pair of vectors to a matrix multiplication. Furthermore, $\mathbf{H}_j^{(k)}$ represents the k-th row of the matrix $\mathbf{H}_j$. The average RF power received by the energy harvester of the j-th receiver is expressed as

$$\overline{P_{EH,j}}\left(\widehat{\mathcal{G}}, \rho_j\right) = \frac{\rho_j}{\mathcal{D}} \sum_{n=1}^{N} \sum_{k=1}^{2L-1} \mathbf{H}_j^{(k)} \mathbf{g}_n \mathbf{g}_n^{\dagger} \mathbf{H}_j^{(k)\dagger} + \rho_j \sigma_z^2, \tag{9}$$

where $\widehat{\mathcal{G}} = [\mathbf{g}_1, \cdots, \mathbf{g}_N]$. The derivation of Eq. (9) is detailed in Appendix B.

The practical EH model uses the diode rectifier circuit to achieve the RF-to-DC conversion. The diode saturation EH model, obtained by fitting the experimental data, has high reality and is widely adopted in both the wideband [41]–[43] and the narrowband [44]–[46] IDET systems. The saturation EH model can be expressed as [42]

$$\begin{aligned} &\Theta(P_{in}) \\ &= \left[\frac{P_{max}}{\exp(-\mu P_{min} + \nu)} \left(\frac{1 + \exp(-\mu P_{min} + \nu)}{1 + \exp(-\mu P_{in} + \nu)} - 1\right)\right]^+, \end{aligned} \tag{10}$$

where μ and ν are the constant parameters with respect to the circuit. P_{min} and P_{max} are the activation and saturation power of the circuit, respectively. P_{in} is the average input RF power and $\Theta(P_{in})$ is the output DC power of the circuit. Moreover, the output DC power at the j-th receiver is expressed as

$$i_j\left(\widehat{\mathcal{G}}, \rho_j\right) = \Theta\left(\overline{P_{EH,j}}\left(\widehat{\mathcal{G}}, \rho_j\right)\right), \text{ [Watt]}. \tag{11}$$

The other portion $\sqrt{1-\rho_j} y_j^{\mathcal{D}}[m]$ of the received signal is exploited for information decoding. After the down-sampling operation, as shown in Fig. 2, the signal $y_{ID,j}[m]$ sent to the information decoder is expressed as [4]

$$\begin{aligned} &y_{ID,j}[m] \\ &= \underbrace{\sqrt{1-\rho_j} \mathbf{H}_j^{(L)} \mathbf{g}_j s_j \left[m - \left\lfloor \frac{L-1}{\mathcal{D}} \right\rfloor\right]}_{\text{Information symbol}} \\ &+ \underbrace{\sqrt{1-\rho_j} \sum_{\substack{p=-\lfloor \frac{L-1}{\mathcal{D}} \rfloor, \\ p\neq 0}}^{\lfloor \frac{L-1}{\mathcal{D}} \rfloor} \mathbf{H}_j^{(L-p\mathcal{D})} \mathbf{g}_j s_j \left[m + p - \left\lfloor \frac{L-1}{\mathcal{D}} \right\rfloor\right]}_{\text{ISI symbol}} \\ &+ \underbrace{\sqrt{1-\rho_j} \sum_{p=-\lfloor \frac{L-1}{\mathcal{D}} \rfloor}^{\lfloor \frac{L-1}{\mathcal{D}} \rfloor} \sum_{\substack{n=1, \\ n\neq j}}^{N} \mathbf{H}_j^{(L-p\mathcal{D})} \mathbf{g}_n s_n \left[m + p - \left\lfloor \frac{L-1}{\mathcal{D}} \right\rfloor\right]}_{\text{IRI symbol}} \\ &+ \sqrt{1-\rho_j} z_j[m] + v_j[m], \end{aligned} \tag{12}$$

where $z_j[m]$ is the down-sampling symbol of $z_j^{\mathcal{D}}[m]$ and $v_j[m]$ is the RF-to-baseband conversion noise with a zero mean and a variance of σ_{cov}^2 [47]. For convenience, we denote the ISI

[4] After power splitting, the receivers decode the symbols by onetap detection [25] and do not need equalization.

symbol power, the IRI symbol power and the Information symbol power as $\overline{P_{ISI,j}}\left(\mathbf{g}_j,\rho_j\right)$, $\overline{P_{IRI,j}}\left(\widehat{\mathcal{G}},\rho_j\right)$ and $\overline{P_{I,j}}\left(\mathbf{g}_j,\rho_j\right)$, which can be expressed as

$$\overline{P_{ISI,j}}\left(\mathbf{g}_j,\rho_j\right)=\left(1-\rho_j\right)\sum_{\substack{p=-\lfloor\frac{L-1}{\mathcal{D}}\rfloor,\\ p\neq 0}}^{\lfloor\frac{L-1}{\mathcal{D}}\rfloor}\mathbf{H}_j^{(L-p\mathcal{D})}\mathbf{g}_j\mathbf{g}_j^{\dagger}\mathbf{H}_j^{(L-p\mathcal{D})\dagger}, \tag{13}$$

$$\overline{P_{IRI,j}}\left(\widehat{\mathcal{G}},\rho_j\right)=\left(1-\rho_j\right)\sum_{p=-\lfloor\frac{L-1}{\mathcal{D}}\rfloor}^{\lfloor\frac{L-1}{\mathcal{D}}\rfloor}\sum_{\substack{n=1,\\ n\neq j}}^{N}\mathbf{H}_j^{(L-p\mathcal{D})}\mathbf{g}_n\mathbf{g}_n^{\dagger}\mathbf{H}_j^{(L-p\mathcal{D})\dagger}, \tag{14}$$

$$\overline{P_{I,j}}\left(\mathbf{g}_j,\rho_j\right)=\left(1-\rho_j\right)\mathbf{H}_j^{(L)}\mathbf{g}_j\mathbf{g}_j^{\dagger}\mathbf{H}_j^{(L)\dagger}. \tag{15}$$

The average power $\overline{P_{ID,j}}\left(\widehat{\mathcal{G}},\rho_j\right)$ of the signal received by the information decoder at the j-th receiver is expressed as

$$\begin{aligned}\overline{P_{ID,j}}\left(\widehat{\mathcal{G}},\rho_j\right)=&\overline{P_{I,j}}\left(\mathbf{g}_j,\rho_j\right)+\overline{P_{ISI,j}}\left(\mathbf{g}_j,\rho_j\right)+\overline{P_{IRI,j}}\left(\widehat{\mathcal{G}},\rho_j\right)\\&+\left(1-\rho_j\right)\sigma_z^2+\sigma_{cov}^2.\end{aligned} \tag{16}$$

The derivations of $y_{ID,j}[m]$ and $\overline{P_{ID,j}}\left(\widehat{\mathcal{G}},\rho_j\right)$ are detailed in Appendix C. The SINR at the information decoder of the j-th receiver is expressed as

$$\begin{aligned}\gamma_j\left(\widehat{\mathcal{G}},\rho_j\right)=&\frac{\overline{P_{I,j}}\left(\mathbf{g}_j,\rho_j\right)}{\overline{P_{ISI,j}}\left(\mathbf{g}_j,\rho_j\right)+\overline{P_{IRI,j}}\left(\widehat{\mathcal{G}},\rho_j\right)+\left(1-\rho_j\right)\sigma_z^2+\sigma_{cov}^2}\\\approx&\frac{\overline{P_{I,j}}\left(\mathbf{g}_j,\rho_j\right)}{\overline{P_{ISI,j}}\left(\mathbf{g}_j,\rho_j\right)+\overline{P_{IRI,j}}\left(\widehat{\mathcal{G}},\rho_j\right)+\sigma_{cov}^2}.\end{aligned} \tag{17}$$

In line with [48], we omit the antenna noise power σ_z^2 in the denominator of Eq. (17) since $\sigma_z^2\ll\sigma_{cov}^2$. Finally, the WDT throughput of the j-th receiver is formulated as [35]

$$R_j\left(\widehat{\mathcal{G}},\rho_j\right)=\frac{B}{\mathcal{D}}\log_2\left(1+\gamma_j\left(\widehat{\mathcal{G}},\rho_j\right)\right),\text{[bit/s]}. \tag{18}$$

III. Downlink Fair-throughput Maximisation

Due to the near-far effect, different receivers in the IDET system have different channel quality. The IDET receivers far away from the transmitter have bad channel quality, which may lead to low throughput and poor service. In order to overcome the near-far effect and ensure the fairness of the IDET system, we formulate the fair-throughput maximisation problem to ensure all the IDET receivers have the same downlink throughput.

A. Problem Formulation

In order to maximise the fair-throughput, the joint waveformer $\widehat{\mathcal{G}}$ and the power splitter $\boldsymbol{\rho}=[\rho_1,\cdots,\rho_N]$ design is formulated as

$$\text{(P1)}:\max_{\widehat{\mathcal{G}},\boldsymbol{\rho}}R_{fair} \tag{19}$$

$$\text{s.t.}\quad R_j\left(\widehat{\mathcal{G}},\rho_j\right)\geq R_{fair},\forall j=1,\cdots,N, \tag{19a}$$

$$i_j\left(\widehat{\mathcal{G}},\rho_j\right)\geq\mathcal{I}_j,\forall j=1,\cdots,N, \tag{19b}$$

$$\sum_{j=1}^{N}\left\|\mathbf{g}_j\right\|_2^2=\mathcal{D}P_{tx}, \tag{19c}$$

$$0\leq\rho_j\leq 1,\forall j=1,\cdots,N. \tag{19d}$$

The constraint (19a) defines the downlink fair-throughput R_{fair}, which is not higher than the downlink throughput of every individual receiver. The constraint (19b) indicates that the output DC power harvested by the j-th receiver should be higher than a minimum threshold $\mathcal{I}_j$. This is a complicated constraint due to the fractional and exponential structures with respect to $\overline{P_{EH,j}}\left(\widehat{\mathcal{G}},\rho_j\right)$ according to Eqs. (10) and (11). Therefore, we transform the constraint (19b) into a linear constraint by transposition as follows

$$\overline{P_{EH,j}}\left(\widehat{\mathcal{G}},\rho_j\right)\geq\widehat{\Theta}\left(\mathcal{I}_j\right),\forall j=1,\cdots,N, \tag{20}$$

where $\widehat{\Theta}\left(\mathcal{I}_j\right)=\frac{1}{\mu}\ln\left(\frac{P_{max}+\mathcal{I}_j\exp\left(-\mu P_{min}+\nu\right)}{\left(P_{max}-\mathcal{I}_j\right)\exp\left(-\mu P_{min}+\nu\right)}\right)+\frac{\nu}{\mu}$. Moreover, (19c) represents the total transmit power constraint and is a non-convex constraint. By introducing the auxiliary variable $\mathbf{p}=[p_1,\cdots,p_N]$, (19c) can be relaxed as follows

$$\left\|\mathbf{g}_j\right\|_2^2\leq p_j,\forall j=1,\cdots,N, \tag{21}$$

$$0\leq\sum_{j=1}^{N}p_j\leq\mathcal{D}P_{tx}. \tag{22}$$

The constraint (19d) represents the range of the power splitting ratio of each receiver.

B. Feasibility of Energy Harvesting

Observe from Eq. (9) that the constraint (20) is still non-convex and the definitional domain of (P1) is also non-convex. Different from classic SDR, we transform (20) into a convex constraint using a MQT method. A fractional function $f(\mathbf{x})$ can be expressed as

$$f(\mathbf{x})=\mathbf{a}^{\dagger}(\mathbf{x})\mathbf{B}^{-1}(\mathbf{x})\mathbf{a}(\mathbf{x}), \tag{23}$$

where we have $\mathbf{a}(\mathbf{x})\in\mathbb{C}^{N\times 1}$ and $\mathbf{B}(\mathbf{x})\in\mathbb{S}_{++}^{N\times N}$. By introducing the auxiliary variable $\mathbf{y}\in\mathbb{C}^{N\times 1}$ and by adopting the QT, Eq. (23) is reformulated as [49]

$$\widehat{f}(\mathbf{x})=2\mathcal{R}\left\{\mathbf{y}^{\dagger}\mathbf{a}(\mathbf{x})\right\}-\mathbf{y}^{\dagger}\mathbf{B}(\mathbf{x})\mathbf{y}. \tag{24}$$

It can be proved that Eq. (24) is equivalent to Eq. (23) by letting $\mathbf{y}=\mathbf{B}^{-1}(\mathbf{x})\mathbf{a}(\mathbf{x})$. Moreover, if $\mathbf{B}(\mathbf{x})$ is a unity matrix, Eq. (23) is reformulated as $f(\mathbf{x})=\mathbf{a}^{\dagger}(\mathbf{x})\mathbf{a}(\mathbf{x})$, which is equivalent to $2\mathcal{R}\left\{\mathbf{y}^{\dagger}\mathbf{a}(\mathbf{x})\right\}-\mathbf{y}^{\dagger}\mathbf{y}$. As a result, in our optimisation, we introduce the auxiliary variable $\boldsymbol{\psi}_{j,n}^{EH}\in\mathbb{C}^{(2L-1)\times 1}$ and the constraint (20) is reformulated as

$$\begin{aligned}\widehat{P}_{EH,j}\left(\widehat{\mathcal{G}},\rho_j,\boldsymbol{\Psi}_j^{EH}\right)=&\frac{\rho_j}{\mathcal{D}}\sum_{n=1}^{N}\left(2\mathcal{R}\left\{\boldsymbol{\psi}_{j,n}^{EH\dagger}\mathbf{a}_{j,n}\right\}-\boldsymbol{\psi}_{j,n}^{EH\dagger}\boldsymbol{\psi}_{j,n}^{EH}\right)+\rho_j\sigma_z^2\\\geq&\widehat{\Theta}\left(\mathcal{I}_j\right),\end{aligned} \tag{25}$$

where $\mathbf{a}_{j,n}=\left[\mathbf{H}_j^{(1)}\mathbf{g}_n,\cdots,\mathbf{H}_j^{(2L-1)}\mathbf{g}_n\right]^T$ and $\boldsymbol{\Psi}_j^{EH}=\left[\boldsymbol{\psi}_{j,1}^{EH},\cdots,\boldsymbol{\psi}_{j,N}^{EH}\right]$. In order to solve (P1), we need to find a feasible solution which satisfies the constraint (25). A new optimisation problem is then formulated as

$$\text{(P2)}:\max_{\widehat{\mathcal{G}},\mathbf{p},\boldsymbol{\Psi}^{EH}}P_{fair} \tag{26}$$

Algorithm 1 MQT based alternating optimisation for (P2).

Input: Channel fading coefficient of $\mathbf{h}_j$; Transmit power of the transmitter P_{tx}; Minimum receiving current I_j; Weighting coefficient ι_j; Error tolerance ϵ.
Output: Feasible solution $\boldsymbol{\Psi}^{EH*}$ and $\widehat{\boldsymbol{\mathcal{G}}}^*$.
1: Initialize $\boldsymbol{\Psi}^{EH} \leftarrow \mathbf{0}$, $P_1 \leftarrow \epsilon$, $P_2 \leftarrow -\epsilon$;
2: **while** $|P_1 - P_2| \geq \epsilon$ **do**
3: $P_2 \leftarrow P_1$;
4: Update $\widehat{\boldsymbol{\mathcal{G}}}^*$ and $\mathbf{p}^*$ by solving (P2-1);
5: Update $\boldsymbol{\psi}_{j,n}^{EH*} \leftarrow \mathbf{a}_{j,n}$;
6: Update $P_1 \leftarrow P_{fair}$;
7: **end while**
8: **return** $\left\{\boldsymbol{\Psi}^{EH*}, \widehat{\boldsymbol{\mathcal{G}}}^*\right\}$.

$$\text{s.t.} \quad \widehat{P}_{EH,j}\left(\widehat{\boldsymbol{\mathcal{G}}}, \rho_j, \boldsymbol{\Psi}_j^{EH}\right) \geq \iota_j P_{fair}, \forall j = 1, \cdots, N, \tag{26a}$$
$$(21), (22),$$

where P_{fair} is the minimum value of $\widehat{P}_{EH,j}\left(\widehat{\boldsymbol{\mathcal{G}}}, \rho_j, \boldsymbol{\Psi}_j^{EH}\right)$ and ι_j is a constant weight. The auxiliary variable $\boldsymbol{\Psi}^{EH} = \left[\boldsymbol{\Psi}_1^{EH}, \cdots, \boldsymbol{\Psi}_N^{EH}\right]$. Unfortunately, (P2) is non-convex with respect to $\widehat{\boldsymbol{\mathcal{G}}}$ and $\boldsymbol{\Psi}^{EH}$. However, we can solve (P2) by alternatively optimising $\widehat{\boldsymbol{\mathcal{G}}}$, $\mathbf{p}$ and $\boldsymbol{\Psi}^{EH}$. First, given a fixed $\boldsymbol{\Psi}^{EH}$, (P2) is reformulated as

$$\text{(P2-1)}: \max_{\widehat{\boldsymbol{\mathcal{G}}}, \mathbf{p}} P_{fair} \tag{27}$$
$$\text{s.t.} \quad (21), (22), (26a),$$

which is a convex problem. By fixing $\widehat{\boldsymbol{\mathcal{G}}}$ and $\mathbf{p}$, (P2) is reformulated as

$$\text{(P2-2)}: \max_{\boldsymbol{\Psi}^{EH}} P_{fair} \tag{28}$$
$$\text{s.t.} \quad (26a).$$

According to Eq. (25), $\widehat{P}_{EH,j}\left(\widehat{\boldsymbol{\mathcal{G}}}, \rho_j, \boldsymbol{\Psi}_j^{EH}\right)$ is convex with respect to the variable $\boldsymbol{\Psi}^{EH}$. Therefore, by letting $\partial \widehat{P}_{EH,j}\left(\widehat{\boldsymbol{\mathcal{G}}}, \rho_j, \boldsymbol{\Psi}_j^{EH}\right) \big/ \partial \boldsymbol{\psi}_{j,n}^{EH} = 0$, the optimal $\boldsymbol{\Psi}^{EH*}$ can be then obtained as $\boldsymbol{\psi}_{j,n}^{EH*} = \mathbf{a}_{j,n}$. The MQT based alternating algorithm is detailed in Algorithm 1. The complexity of the Algorithm 1 solved by the interior-point method is $O\left(N_1 L^{3.5}\right)$ [50], where N_1 is the maximum number of iterations required in Algorithm 1.

C. Waveforming Design

After obtaining a feasible value of $\widehat{P}_{EH,j}\left(\widehat{\boldsymbol{\mathcal{G}}}, \rho_j, \boldsymbol{\Psi}_j^{EH}\right)$, we then solve (P1) and design the optimal waveformer and power splitter. Observe from Eqs. (13)-(18) that the variables $\mathbf{g}_j$ and ρ_j are both in the numerator and denominator, when calculating the throughput $R_j\left(\widehat{\boldsymbol{\mathcal{G}}}, \rho_j\right)$. Therefore, (P1) is a FP problem. By adopting the QT and introducing the auxiliary variable $\psi_j^{ID} \in \mathbb{C}^{1\times 1}$, (P1) is reformulated as

$$\text{(P3)}: \max_{\widehat{\boldsymbol{\mathcal{G}}}, \boldsymbol{\rho}, \mathbf{p}, \boldsymbol{\Psi}^{EH}, \boldsymbol{\Psi}^{ID}} \widetilde{R}_{fair} \tag{29}$$
$$\text{s.t.} \quad \widetilde{R}_j\left(\widehat{\boldsymbol{\mathcal{G}}}, \rho_j, \psi_j^{ID}\right) \geq \widetilde{R}_{fair}, \forall j = 1, \cdots, N, \tag{29a}$$
$$(19d), (21), (22), (25),$$

where $\boldsymbol{\Psi}^{ID} = \left[\psi_1^{ID}, \cdots, \psi_N^{ID}\right]$ and $\widetilde{R}_{fair}$ is the downlink fair-throughput obtained by (P3). The throughput $\widetilde{R}_j\left(\widehat{\boldsymbol{\mathcal{G}}}, \rho_j, \psi_j^{ID}\right)$ is expressed as

$$\widetilde{R}_j\left(\widehat{\boldsymbol{\mathcal{G}}}, \rho_j, \psi_j^{ID}\right) = \frac{B}{\mathcal{D}} \log_2\Big(1 + 2\sqrt{1-\rho_j}\mathcal{R}\left\{\psi_j^{ID\dagger}\mathbf{H}_j^{(L)}\mathbf{g}_j\right\} - \psi_j^{ID}\psi_j^{ID\dagger}\left[\overline{P_{ISI,j}}\left(\mathbf{g}_j, \rho_j\right) + \overline{P_{IRI,j}}\left(\widehat{\boldsymbol{\mathcal{G}}}, \rho_j\right) + \sigma_{cov}^2\right]\Big). \tag{30}$$

We solve (P3) by iteratively optimising the variables $\widehat{\boldsymbol{\mathcal{G}}}$, $\boldsymbol{\rho}$, $\mathbf{p}$, $\boldsymbol{\Psi}^{EH}$ and $\boldsymbol{\Psi}^{ID}$. First, given fixed $\boldsymbol{\rho}$, $\boldsymbol{\Psi}^{EH}$ and $\boldsymbol{\Psi}^{ID}$, (P3) is reformulated as

$$\text{(P3-1)}: \max_{\widehat{\boldsymbol{\mathcal{G}}}, \mathbf{p}} \widetilde{R}_{fair} \tag{31}$$
$$\text{s.t.} \quad (21), (22), (25), (29a).$$

Then, when we fix $\widehat{\boldsymbol{\mathcal{G}}}$, $\mathbf{p}$, $\boldsymbol{\Psi}^{EH}$ and $\boldsymbol{\Psi}^{ID}$, (P3) is reformulated as

$$\text{(P3-2)}: \max_{\boldsymbol{\rho}} \widetilde{R}_{fair} \tag{32}$$
$$\text{s.t.} \quad (19d), (25), (29a).$$

Since (P3-1) and (P3-2) are both convex, the optimal $\widehat{\boldsymbol{\mathcal{G}}}^*$, $\boldsymbol{\rho}^*$ and $\mathbf{p}^*$ can be readily obtained. Then, given fixed $\widehat{\boldsymbol{\mathcal{G}}}$, $\mathbf{p}$, $\boldsymbol{\rho}$ and $\boldsymbol{\Psi}^{ID}$, (P3) is reformulated as

$$\text{(P3-3)}: \max_{\boldsymbol{\Psi}^{EH}} \widetilde{R}_{fair} \tag{33}$$
$$\text{s.t.} \quad (25).$$

By letting $\partial \widehat{P}_{EH,j}\left(\widehat{\boldsymbol{\mathcal{G}}}, \rho_j, \boldsymbol{\Psi}_j^{EH}\right) \big/ \partial \boldsymbol{\psi}_{j,n}^{EH} = 0$, the optimal $\boldsymbol{\Psi}^{EH*}$ can then be obtained as $\boldsymbol{\psi}_{j,n}^{EH*} = \mathbf{a}_{j,n}$. Finally, given fixed $\widehat{\boldsymbol{\mathcal{G}}}$, $\mathbf{p}$, $\boldsymbol{\rho}$ and $\boldsymbol{\Psi}^{EH}$, (P3) is reformulated as

$$\text{(P3-4)}: \max_{\boldsymbol{\Psi}^{ID}} \widetilde{R}_{fair} \tag{34}$$
$$\text{s.t.} \quad (29a).$$

Since (P3-4) is convex, by letting $\partial \widetilde{R}_j\left(\widehat{\boldsymbol{\mathcal{G}}}, \rho_j, \psi_j^{ID}\right) \big/ \partial \psi_j^{ID} = 0$, we can obtain the optimal $\boldsymbol{\Psi}^{ID*}$, which can be expressed as

$$\psi_j^{ID*} = \frac{\sqrt{1-\rho_j}\mathbf{H}_j^{(L)}\mathbf{g}_j}{\overline{P_{ISI,j}}\left(\mathbf{g}_j, \rho_j\right) + \overline{P_{IRI,j}}\left(\widehat{\boldsymbol{\mathcal{G}}}, \rho_j\right) + \sigma_{cov}^2}. \tag{35}$$

The FP based alternating optimisation is detailed in Algorithm 2. By alternatively optimising the convex sub-problems (P3-1)-(P3-4), the iteration of Algorithm 2 from Line 2 to Line

Algorithm 2 FP based alternating optimisation for (P1).

Input: Feasible solution $\boldsymbol{\Psi}^{EH}$; Auxiliary variable $\boldsymbol{\Psi}^{ID}$; Transmit power of the transmitter P_{tx}; Error tolerance ϵ.
Output: Optimal waveformer $\widehat{\boldsymbol{\mathcal{G}}}^*$; Optimal power splitter $\boldsymbol{\rho}^*$; Optimal fair-throughput R_{fair}^*.
1: Initialize $\boldsymbol{\rho} \leftarrow \mathbf{1}$, $\widehat{R}_1 \leftarrow \epsilon$, $\widehat{R}_2 \leftarrow -\epsilon$;
2: **while** $\left|\widehat{R}_1 - \widehat{R}_2\right| \geq \epsilon$ **do**
3: $\widehat{R}_2 \leftarrow \widehat{R}_1$;
4: Update $\widehat{\boldsymbol{\mathcal{G}}}^*$ and $\mathbf{p}^*$ by solving (P3-1);
5: Update $\boldsymbol{\rho}^*$ by solving (P3-2);
6: Update $\boldsymbol{\psi}_{j,n}^{EH*} \leftarrow \mathbf{a}_{j,n}$;
7: Update $\boldsymbol{\Psi}^{ID*}$ by Eq. (35);
8: Update $\widehat{R}_1 \leftarrow \widetilde{R}_{fair}$;
9: **end while**
10: Update $R_{fair}^* \leftarrow \widetilde{R}_{fair}$;
11: **return** $\left\{\widehat{\boldsymbol{\mathcal{G}}}^*, \boldsymbol{\rho}^*, R_{fair}^*\right\}$.

9 converges to the global optimal solution to (P3) [51], which is a stationary point to non-convex (P1). The convergence of Algorithm 2 is demonstrated in Appendix D. When we solve (P3) by the interior-point method, the complexity of Algorithm 2 is $O\left(N^F L^{3.5}\right)$ [50], where N^F is the maximum number of iterations required in Algorithm 2.

IV. Downlink sum-throughput maximisation

In order to exploit the resource of the communication system up to the hilt, the sum-throughput is used to evaluate the data transmission efficiency.

A. Problem Formulation

The downlink sum-throughput maximisation problem can be formulated as

$$\begin{aligned}(\text{P4}): \max_{\widehat{\boldsymbol{\mathcal{G}}},\boldsymbol{\rho},\mathbf{p}} \; & R_{sum}\left(\widehat{\boldsymbol{\mathcal{G}}},\boldsymbol{\rho}\right) \\ \text{s.t.} \quad & (19b),(19d),(21),(22),\end{aligned} \tag{36}$$

where $R_{sum}\left(\widehat{\boldsymbol{\mathcal{G}}},\boldsymbol{\rho}\right) = \sum_{j=1}^{N} R_j\left(\widehat{\boldsymbol{\mathcal{G}}},\rho_j\right)$ is the sum-throughput. Similarly, by adopting the QT and the MQT, (P4) is reformulated as

$$\begin{aligned}(\text{P5}): \max_{\widehat{\boldsymbol{\mathcal{G}}},\boldsymbol{\rho},\mathbf{p},\boldsymbol{\Psi}^{EH},\boldsymbol{\Psi}^{ID}} \; & \widetilde{R}_{sum}\left(\widehat{\boldsymbol{\mathcal{G}}},\boldsymbol{\rho},\boldsymbol{\Psi}^{ID}\right) \\ \text{s.t.} \quad & (19d),(21),(22),(25),\end{aligned} \tag{37}$$

where $\widetilde{R}_{sum}\left(\widehat{\boldsymbol{\mathcal{G}}},\boldsymbol{\rho},\boldsymbol{\Psi}^{ID}\right) = \sum_{j=1}^{N} \widetilde{R}_j\left(\widehat{\boldsymbol{\mathcal{G}}},\rho_j,\psi_j^{ID}\right)$. By alternatively optimising $\widehat{\boldsymbol{\mathcal{G}}}$, $\boldsymbol{\rho}$, $\mathbf{p}$, $\boldsymbol{\Psi}^{EH}$ and $\boldsymbol{\Psi}^{ID}$, (P5) converges to an optimal point, which is a stationary point of (P4). First, given fixed $\boldsymbol{\rho}$, $\boldsymbol{\Psi}^{EH}$ and $\boldsymbol{\Psi}^{ID}$, (P5) is equivalent to

$$\begin{aligned}(\text{P5-1}): \max_{\widehat{\boldsymbol{\mathcal{G}}},\mathbf{p}} \; & \widetilde{R}_{sum}\left(\widehat{\boldsymbol{\mathcal{G}}},\boldsymbol{\rho},\boldsymbol{\Psi}^{ID}\right) \\ \text{s.t.} \quad & (21),(22),(25).\end{aligned} \tag{38}$$

By fixing $\widehat{\boldsymbol{\mathcal{G}}}$, $\mathbf{p}$, $\boldsymbol{\Psi}^{EH}$ and $\boldsymbol{\Psi}^{ID}$, (P5) is equivalent to

$$\begin{aligned}(\text{P5-2}): \max_{\boldsymbol{\rho}} \; & \widetilde{R}_{sum}\left(\widehat{\boldsymbol{\mathcal{G}}},\boldsymbol{\rho},\boldsymbol{\Psi}^{ID}\right) \\ \text{s.t.} \quad & (19d),(25).\end{aligned} \tag{39}$$

The sub-problems (P5-1) and (P5-2) are both convex. We are capable of solving them by any convex optimisation tool. Given fixed $\widehat{\boldsymbol{\mathcal{G}}}$, $\boldsymbol{\rho}$, $\mathbf{p}$ and $\boldsymbol{\Psi}^{ID}$, (P5) is equivalent to

$$\begin{aligned}(\text{P5-3}): \max_{\boldsymbol{\Psi}^{EH}} \; & \widetilde{R}_{sum}\left(\widehat{\boldsymbol{\mathcal{G}}},\boldsymbol{\rho},\boldsymbol{\Psi}^{ID}\right) \\ \text{s.t.} \quad & (25).\end{aligned} \tag{40}$$

Similar to (P3-3), the optimal solution of (P5-3) is expressed as $\boldsymbol{\psi}_{j,n}^{EH*} = \mathbf{a}_{j,n}$. Finally, given fixed $\widehat{\boldsymbol{\mathcal{G}}}$, $\boldsymbol{\rho}$, $\mathbf{p}$ and $\boldsymbol{\Psi}^{EH}$, (P5) is reformulated as

$$(\text{P5-4}): \max_{\boldsymbol{\Psi}^{ID}} \widetilde{R}_{sum}\left(\widehat{\boldsymbol{\mathcal{G}}},\boldsymbol{\rho},\boldsymbol{\Psi}^{ID}\right). \tag{41}$$

By letting $\partial \widetilde{R}_{sum}\left(\widehat{\boldsymbol{\mathcal{G}}},\boldsymbol{\rho},\boldsymbol{\Psi}^{ID}\right) \Big/ \partial \psi_j^{ID} = 0$, we can obtain the optimal $\boldsymbol{\Psi}^{ID*}$ which is the same as Eq. (35).

The alternating optimisation for maximising the sum-throughput is detailed in Algorithm 3. By alternatively optimising the convex sub-problems (P5-1)-(P5-4), the iteration of Algorithm 3 from Line 2 to Line 9 converges to the local optimal solution to (P5) [49], which is a stationary point to non-convex (P4). The proof for the convergence of Algorithm 3 is similar to Algorithm 2. Similarly, the complexity of Algorithm 3 is $O\left(N^S L^{3.5}\right)$, where N^S is the maximum number of iterations required in Algorithm 3.

Algorithm 3 FP based alternating optimisation for (P4).

Input: Feasible solution $\boldsymbol{\Psi}^{EH}$; Auxiliary variable $\boldsymbol{\Psi}^{ID}$; Transmit power of the transmitter P_{tx}; Error tolerance ϵ.
Output: Optimal waveformer $\widehat{\boldsymbol{\mathcal{G}}}^*$; Optimal power splitter $\boldsymbol{\rho}^*$; Optimal sum-throughput $R_j^*\left(\widehat{\boldsymbol{\mathcal{G}}}^*,\boldsymbol{\rho}^*\right)$.
1: Initialize $\boldsymbol{\rho} \leftarrow \mathbf{1}$, $\widehat{R}_1 \leftarrow \epsilon$, $\widehat{R}_2 \leftarrow -\epsilon$;
2: **while** $\left|\widehat{R}_1 - \widehat{R}_2\right| \geq \epsilon$ **do**
3: $\quad \widehat{R}_2 \leftarrow \widehat{R}_1$;
4: $\quad$ Update $\widehat{\boldsymbol{\mathcal{G}}}^*$ and $\mathbf{p}^*$ by solving (P5-1);
5: $\quad$ Update $\boldsymbol{\rho}^*$ by solving (P5-2);
6: $\quad$ Update $\boldsymbol{\psi}_{j,n}^{EH*} \leftarrow \mathbf{a}_{j,n}$;
7: $\quad$ Update $\boldsymbol{\Psi}^{ID*}$ by Eq. (35);
8: $\quad$ Update $\widehat{R}_1 \leftarrow \widetilde{R}_{sum}\left(\widehat{\boldsymbol{\mathcal{G}}}^*,\boldsymbol{\rho}^*,\boldsymbol{\Psi}^{ID*}\right)$;
9: **end while**
10: Update $R_{sum}\left(\widehat{\boldsymbol{\mathcal{G}}}^*,\boldsymbol{\rho}^*\right) \leftarrow \widetilde{R}_{sum}\left(\widehat{\boldsymbol{\mathcal{G}}}^*,\boldsymbol{\rho}^*,\boldsymbol{\Psi}^{ID*}\right)$;
11: **return** $\left\{\widehat{\boldsymbol{\mathcal{G}}}^*,\boldsymbol{\rho}^*,R_{sum}^*\left(\widehat{\boldsymbol{\mathcal{G}}}^*,\boldsymbol{\rho}^*\right)\right\}$.

V. Simulation Results

A. Parameter Settings

The transmit power is $P_{tx} = 38$ dBm. The carrier frequency is $f_c = 1.5$ GHz and the bandwidth is $B = 125$ MHz [36]. The transmit antenna gain and the receive antenna gain are $G_t = G_r = 1.6$ [36]. The path-loss exponent is $\beta = 3$ [36]. The channel length is $L = 20$ and the RMS delay spread is $15T_s$ for all receivers [5] [32]. The parameters of the EH model are $P_{min} = 0.064$ mW, $P_{max} = 4.927$ mW, $\mu = 274$ and $\nu = 0.29$ [42]. The output DC power is $\mathcal{I}_j = -11$ dBm. The distance between the transmitter and the receivers is 1.5 m. The error tolerance is $\epsilon = 10^{-5}$. All of the simulation results are obtained by averaging the randomness of the channel coefficients.

In the following section, we investigate the performance of the following schemes:

- *Optimal Solution (OPT)* scheme, which is obtained by Algorithm 2 or Algorithm 3;
- *SDR* scheme, whose optimal waveformer is obtained by SDR and is detailed in [52];
- *Minimum Mean Square Error (MMSE)* scheme, whose waveformer $\mathbf{g}_{MMSE,j}$ can be expressed as [31]

$$\begin{aligned}&\mathbf{g}_{MMSE,j} \\ =&c_j^{MMSE}\sqrt{p_j}\left(\sum_{q=1}^{N} p_q \mathbf{H}_{ID,q}^{\dagger}\mathbf{H}_{ID,q} + \sigma_{cov}^2\mathbf{I}\right)^{-1}\mathbf{H}_j^{(L)\dagger}.\end{aligned} \tag{42}$$

Note that c_k^{MMSE} is the constant factor and $\left\|\mathbf{g}_{MMSE,j}\right\|_2^2 = p_j$. $\mathbf{I}$ is an $L \times L$ identity matrix. We can obtain a near-optimal throughput in the WDT scenario by using the MMSE waveformer. Similar to Algorithm 2 and

[5] In the real world, the RMS delay spread of the different receivers is different, as it is influenced by factors such as the signal transmission path, receiver location and movement speed [34]. However, for convenience, we let all the receivers have the same RMS delay spread.

Algorithm 3, we can obtain the optimal fair-throughput and sum-throughput with the MMSE waveformer.

- *Zero Force (ZF)* scheme, whose waveformer $\mathbf{g}_{ZF,j}$ can be expressed as

$$\mathbf{g}_{ZF,j} = c_j^{ZF} \sqrt{p_j} \left(\sum_{q=1}^{N} \mathbf{H}_{ID,q}^{\dagger} \mathbf{H}_{ID,q} \right)^{-1} \mathbf{H}_j^{(L)\dagger}, \quad (43)$$

where c_j^{ZF} is the constant factor and $\|\mathbf{g}_{ZF}\|_2^2 = p_j$ [30].

- *Time-Reversal (TR)* scheme, whose waveformer can be expressed as [28]

$$\mathbf{g}_{TR,j} = \sqrt{p_j} \mathbf{H}_j^{(L)\dagger} \Big/ \left\| \mathbf{H}_j^{(L)\dagger} \right\|_2. \quad (44)$$

- *SISO-OFDMA* scheme [53], which is proposed by using the same wideband resolvable channel model in this paper. The SISO-OFDMA transmitter and all the receivers are deployed with a single antenna. In order to ensure fairness, the transmit power of our OFDMA counterpart is set to P_{tx} in the time domain for fairness, which is detailed in [53]. The bandwidth for the SISO-OFDM system is B = 125 MHz, while the number of subcarriers is 128 [23].
- *MISO-OFDMA* scheme [53], where the transmitter is deployed with two antennas and all the receivers are deployed with a single antenna. The simulation parameters of the MISO-OFDMA scheme are the same as that of the SISO-OFDMA scheme.
- *WSP*, which refers to exist the individual subcarrier power constraint for the practical OFDMA scheme.
- *WOSP*, which refers to do not exist the individual subcarrier power constraint for the OFDMA scheme.

TABLE I
COMPLEXITIES OF THE DIFFERENT ALGORITHMS

Technology	(P1)	(P4)
SDR	$O\left(N_{SDR}^{F} L^{7}\right)$	$O\left(N_{SDR}^{S} L^{7}\right)$
OPT	$O\left(N^{F} L^{3.5}\right)$	$O\left(N^{S} L^{3.5}\right)$

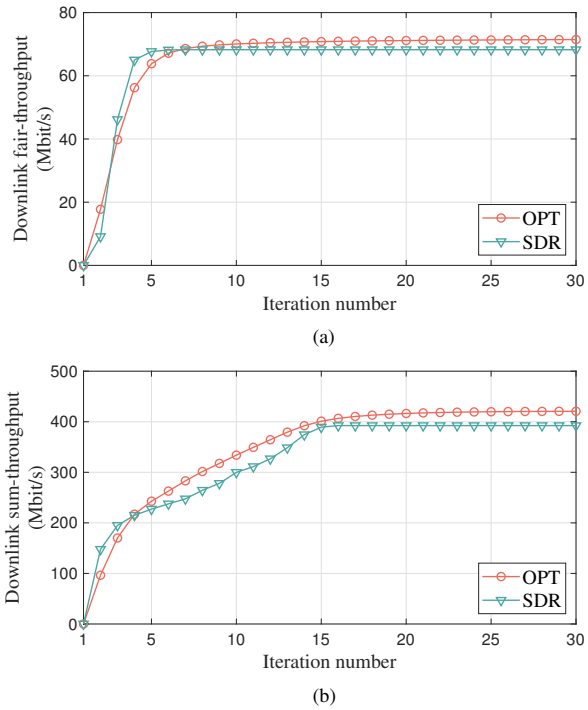

Fig. 3. The convergence of FP based alternating optimisation algorithm: (a) downlink fair-throughput; (b) downlink sum-throughput.

B. Convergence of the Algorithm

We first study the convergence of our proposed FP based alternating optimisation algorithms in Fig. 3. Observe from Figs. 3(a) and 3(b) that the fair-throughput and sum-throughput of our low complexity OPT schemes converge within 15 and 25 iterations, respectively. Simultaneously, the fair-throughput and the sum-throughput by adopting the SDR schemes converge within 7 and 17 iterations. By exploiting the SDR technique, (P1) and (P4) converge to a global optimal point [49] and a stationary point [54], respectively. Our proposed algorithms converge to stationary points close to the SDR schemes, which indicates the effectiveness of our proposed algorithms. We compare the complexities of the different algorithms in TABLE I. N_{SDR}^{F} and N_{SDR}^{S} are the maximum number of iterations when we solve (P1) and (P4) with the SDR schemes, respectively. When the iteration number satisfies $N_{SDR}^{F} \approx N^{F}$ and $N_{SDR}^{S} \approx N^{S}$, our proposed algorithms have lower complexities. Therefore, Our OPT scheme outperforms the SDR counterparts.

C. Individual Downlink Throughput

In order to demonstrate the difference between the downlink fair-throughput and sum-throughput maximisation, we plot the individual throughput attained by 3 receivers in Fig. 4. The distance between the transmitter and the receivers is set as 1.5 m, 2 m and 2.5 m in sequence. Observe from Fig. 4 that when we aim at maximising the sum-throughput, the downlink throughputs from Receiver 1 to Receiver 3 are decreasing in order obviously. This is because the receiver close to the transmitter can achieve a higher signal power gain, which leads to a higher throughput. In order to maximise the sum-throughput, more power is assigned to the receivers close to the transmitter, which results in considerable unfairness. Furthermore, observe from Fig. 4 that all the receivers can reach almost the same throughput, when we maximise the downlink fair-throughput. In order to achieve this objective, more power is allocated to the receivers which are far away from the transmitter to overcome the severe path-loss. As a result, the performance of the downlink sum-throughput is inevitably sacrificed.

D. Number of Resolvable Paths

Increasing the number of scatterers in the environment increases the number of resolvable transmission paths. By setting the RMS delay spread of all the receivers as $\{10T_s, 15T_s, 20T_s\}$ in sequence, we study the impact of the number of resolvable transmission paths on the downlink fair-throughput and sum-throughput in Figs. 5(a) and 5(b), respectively.

This article has been accepted for publication in IEEE Transactions on Wireless Communications. This is the author's version which has not been fully edited and content may change prior to final publication. Citation information: DOI 10.1109/TWC.2023.3303415

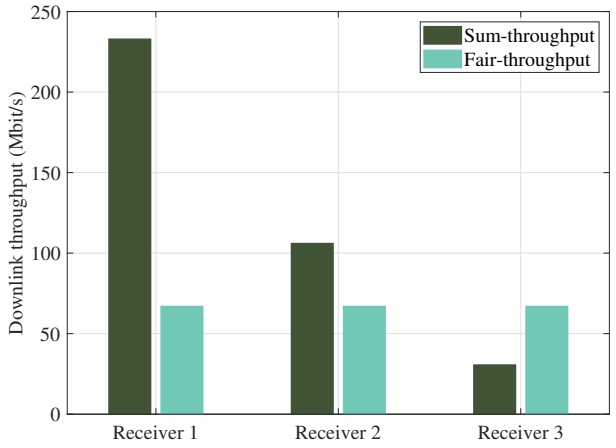

Fig. 4. Individual receiver throughput.

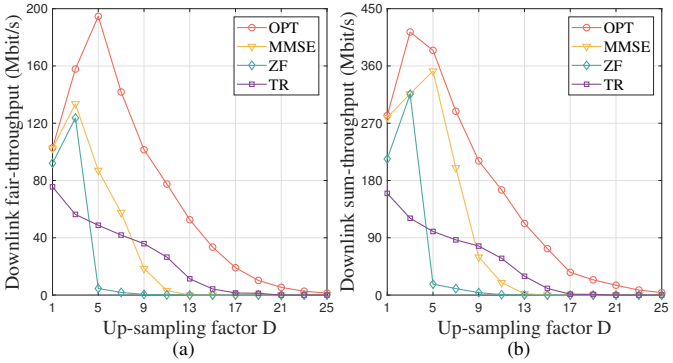

Fig. 6. The impact of the sampling factor on the WDT throughput: (a) fair-throughput; (b) sum-throughput.

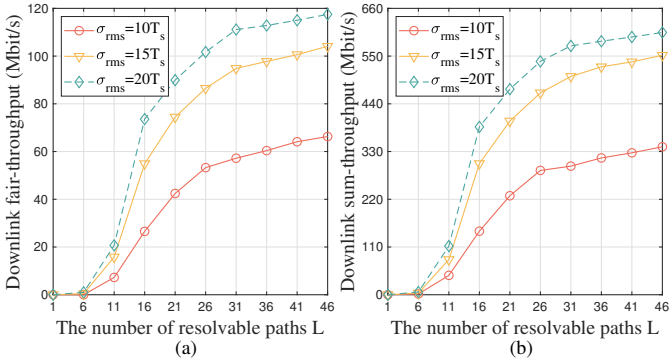

Fig. 5. The impact of the number of the resolvable paths on the WDT downlink throughput: (a) fair-throughput; (b) sum-throughput.

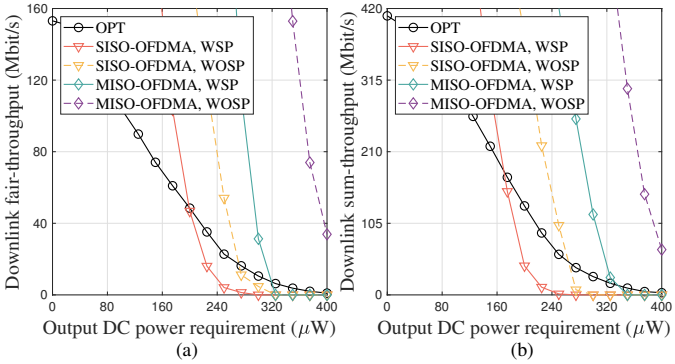

Fig. 7. Trade-off between the WDT and the WDT performance, under the number of the subcarrier is 128 and the power of the individual subcarrier power constraint $P^{peak} = 2P_{tx}$ in WOSP scheme. : (a) fair-throughput; (b) sum-throughput.

Observe from Fig. 5(a) that the downlink fair-throughput rapidly increases as we increase the number of resolvable transmission paths to 31, while the sum-throughput also rapidly increases as we increase the number of resolvable transmission paths to 26, as shown in Fig. 5(b). Finally, both the fair-throughput and sum-throughput increase slowly as we continuously increase the number of resolvable transmission paths. This is because the spatial gain of all the receivers improves as we initially increase the resolvable transmission paths. However, when we continuously increase the number of resolvable paths, the ISI and IRI become dominant, which then constrains the improvement in the fair-throughput and the sum-throughput. Moreover, both the fair-throughput and the sum-throughput improve as the RMS delay spread $\widetilde{\tau}_{rms}$ increases. Observe from Eq. (3) that when we increase $\widetilde{\tau}_{rms}$, the variance of the small-scale fading increases. Therefore, the average power gain of each resolvable path increases.

E. Up-Sampling Factor

By setting the sampling factor $\mathcal{D}$ from 1 to 25, we study its impact on the downlink fair-throughput and sum-throughput in Figs. 6(a) and 6(b), respectively. Observe from Fig. 6(a) that as we increase the up-sampling factor to 5, the downlink fair-throughput attained by Algorithm 2 gradually increases. By contrast, it reduces as we further increase the up-sampling factor. We also observe a similar trend with the MMSE waveformer and the ZF waveformer. However, the fair-throughput associated with a TR waveformer monotonously reduces, as we increase the up-sampling factor. This is because there is a trade-off between the sampling factor and the SINR. Observe from Eqs. (17)-(18), the denominator terms $\gamma_j\left(\widehat{\boldsymbol{\mathcal{G}}}, \rho_j\right)$ reduce, when the sampling factor increases, which results in the increase of the throughput. However, observe from Eq. (18) that increasing the up-sampling factor $\mathcal{D}$ in the denominator will restrain the increase of throughput for receivers. Furthermore, observe from Eqs. (9) and (10) that in order to satisfy the harvested DC requirement of the receiver, as expressed in Eq. (19b), the receivers have to allocate more energy to their energy harvesters, as the up-sampling factor $\mathcal{D}$ increases. As a result, the downlink fair-throughput first increases but then decreases as it achieves its peak, and finally converges to 0. The similar trend is also observed in Fig. 6(b), when we optimise the downlink sum-throughput as shown in Fig. 6(b). Furthermore, we may also observe from Fig. 6 that our proposed solution significantly outperforms the MMSE, ZF and TR counterparts.

F. Output DC Power Requirement

The impact of the output DC power requirement on both the downlink fair-throughput and the sum-throughput is illustrated in Figs. 7(a) and 7(b), respectively. Observe from Figs. 7(a) and 7(b) that the downlink fair-throughput and sum-throughput decrease and converge to 0, as we increase the output DC power requirement. This is because the receivers allocate less signal power to the information decoder, if we increase the output DC power requirement. As a result, when the output DC power requirement is very high, the receivers may allocate all the signal power for energy harvesting.

In Fig. 7(a), we also compare the SISO-OFDMA and MISO-OFDMA counterparts with our OPT scheme. When the output DC power requirement is lower than 200 μW, both the SISO-OFDMA and MISO-OFDMA counterparts achieve higher WDT throughput than our OPT scheme. This is because the OFDM waveform may eliminate ISI, which leads to higher throughput performance. Moreover, for a practical OFDMA system with the individual subcarrier power constraint [55], when we have high output DC power requirement, our OPT scheme outperforms the SISO-OFDMA and MISO-OFDMA counterparts. This is because the subcarrier power constraint limits the WET performance of the OFDMA. Especially, when we remove the individual subcarrier power constraint and have a high output DC power requirement, the WDT performance of our OPT scheme outperforms the SISO-OFDMA counterpart. This is because the cyclic prefix symbol of OFDM carries low power and occupies about $1/6$ period over a whole OFDM period, which leads to lower WET performance. When the output DC requirement is high, the SISO-OFDMA scheme needs more received RF power for energy harvesting and the WDT performance decreases rapidly. After waveforming, the WET performance of our OPT scheme outperforms the SISO-OFDMA counterpart, which results in a higher WDT performance with a high output DC power requirement. The IDET performance of the MISO-OFDMA counterpart without the individual subcarrier power constraint outperforms our OPT scheme. This is because the spatial gain obtained from the MISO outperforms the spatial gain obtained from the wideband multipath channel.

G. Transmit Power

By setting $\mathcal{D} = 1$, we study the impact of the transmit power constraint P_{tx} on both the downlink fair-throughput and the sum-throughput in Figs. 8(a) and 8(b), respectively. As increasing P_{tx} from 34 dBm to 37 dBm, the fair-throughput increases quickly. When we further increase P_{tx} beyond 38 dBm, the fair-throughput increases slowly and finally converges. We have similar trend when optimises the sum-throughput. Observe from Eqs. (16)-(18), the information, the ISI and the IRI signal power increase as we increase P_{tx}. When P_{tx} is low, the information signal power increases more quickly than the others. Therefore, the downlink throughput substantially increases. However, when P_{tx} is high, the downlink throughput will be suppressed by the increasing ISI and the IRI power. As a result, the downlink fair-throughput and sum-throughput increase slowly and finally converge.

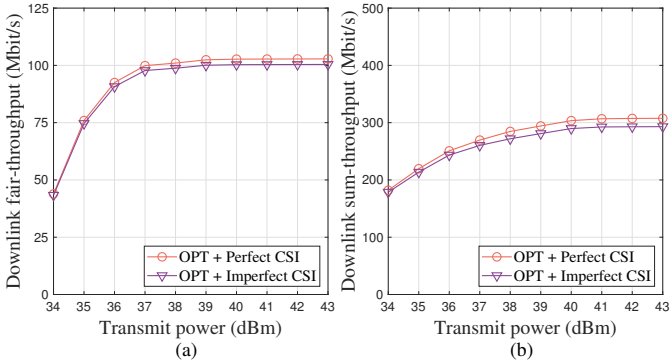

Fig. 8. The impact of the transmit power on the throughput, under the RMS delay spread is $15T_s$, the resolvable paths $L = 20$, the output DC power requirement $\mathcal{I}_j = -11$ dBm and the up-sampling factor $\mathcal{D} = 1$.: (a) fair-throughput; (b) sum-throughput.

In addition, we evaluate the WDT performance in the imperfect CSI case. We assume the perfect CSI $\mathbf{h}_j$ lies in a ball with radius $0.1\left\|\mathbf{h}_j\right\|_2$ around the imperfect CSI $\tilde{\mathbf{h}}_j$, i.e., $\mathbf{h}_j = \left\{\tilde{\mathbf{h}}_j + \boldsymbol{\delta}_j \middle| \left\|\boldsymbol{\delta}_j\right\|_2 \leq 0.1\left\|\mathbf{h}_j\right\|_2\right\}$, where $\boldsymbol{\delta}_j$ is the channel estimation error of the j-th receiver [56]. It can be seen in Figs. 8(a) and 8(b) that the fair-throughput and the sum-throughput with the imperfect CSI are slightly small than the perfect CSI cases, indicating the robustness of our OPT algorithms with the channel estimation errors.

VI. Conclusion

In this paper, we studied wideband waveforming for IDET. In order to improve the IDET performance with less hardware complexity, the spatial gain provided by multiple resolvable transmission paths was exploited. By adopting QT and MQT, a FP based alternating algorithm was relied upon for optimising the waveformers in order to maximise the downlink fair-throughput and the sum-throughput of all the IDET receivers. According to our simulation results, we could substantially improve the IDET performance by exploiting this additional spatial gain, which is suitable for the scenario with abundant resolvable transmission paths. Moreover, our proposed FP based waveforming design substantially outperforms the MMSE, the ZF and the TR counterparts in terms of the IDET performance. Our scheme outperforms the SISO-OFDMA scheme when we have a high output DC requirement. And when we have an individual subcarrier power constraint, our scheme outperforms the MISO-OFDMA scheme.

Appendix A
Proof of the Theorem 1

Denote the total transmit period for sending $\mathbf{s}_j^{\mathcal{D}}$ as $T = (M\mathcal{D} + L - 1)T_s$. Denote the transmit symbol sequence as $\mathbf{x}_j = \mathbf{s}_j^{\mathcal{D}} * \mathbf{g}_j = \mathbf{S}_j^{\mathcal{D}}\mathbf{g}_j$, where $\mathbf{S}_j^{\mathcal{D}} \in \mathbb{C}^{(M\mathcal{D}+L-1)\times(L-1)}$ is the Toeplitz matrix with the vector $\left[\left(\mathbf{s}_j^{\mathcal{D}}\right)^T, \mathbf{0}^T\right]^T$ as its first column.

The average transmit power of the transmit antenna P_{tx} can be expressed as

$$\begin{aligned} P_{tx} &= \frac{T_s}{T}\sum_{j}\sum_{p=1}^{M\mathcal{D}+L-1}\mathbb{E}\left[\left|\mathbf{S}_j^{\mathcal{D}(p)}\mathbf{g}_j\right|^2\right] \\ &= \frac{1}{M\mathcal{D}+L-1}\sum_{j}\sum_{m=0}^{M\mathcal{D}-1}\mathbb{E}\left[\left|s_j^{\mathcal{D}}[m]\right|^2\sum_{l=0}^{L-1}\left|g_j[l]\right|^2\right] \\ &= \frac{1}{M\mathcal{D}+L-1}\sum_{j}\left\|\mathbf{g}_j\right\|_2^2\sum_{m=0}^{M-1}\left|s_j[m]\right|^2 \\ &= \frac{M}{M\mathcal{D}+L-1}\sum_{j}\left\|\mathbf{g}_j\right\|_2^2. \end{aligned} \tag{45}$$

In practice, we have $M \gg L$ [39] and $\mathcal{D} \geq 1$, which indicate that $\sum_j \left\|\mathbf{g}_j\right\|_2^2 = \mathcal{D}P_{tx}$.

Appendix B
Average Power Expression Eq. (9) of Energy Harvester.

Define the index as $m = m_1 + q$, where m_1 satisfies mod $(m_1, \mathcal{D}) = 0$ and q belongs to the set $\{q|0 \leq q \leq \mathcal{D}-1, q \in \mathbb{N}\}$. Since the row index k of the Toeplitz matrix $\mathbf{H}_j$ satisfies $1 \leq k \leq 2L-1$, we obtain

$$-\frac{q+2-2L}{\mathcal{D}} \leq \frac{q-k+1}{\mathcal{D}} \leq \frac{q}{\mathcal{D}}. \tag{46}$$

Observe from Eq. (6) and Eq. (8) that only if mod $(q-k+1, \mathcal{D}) = 0$, the symbol $s_j^{\mathcal{D}}[m_1+q-k+1]$ is non-zero. Thus, the inequality (46) can be reformulated as

$$\left\lceil\frac{q+2-2L}{\mathcal{D}}\right\rceil \leq \frac{q-k+1}{\mathcal{D}} \leq \left\lfloor\frac{q}{\mathcal{D}}\right\rfloor = 0. \tag{47}$$

The index k is constrained by $k_{q,1} \leq k \leq k_{q,2}$, where $k_{q,1}$ and $k_{q,2}$ are denoted as

$$k_{q,1} = q+1, \tag{48}$$

$$k_{q,2} = q+1+\mathcal{D}\left\lfloor\frac{2L-q-2}{\mathcal{D}}\right\rfloor, \tag{49}$$

respectively. Let $\mathbf{H}_{j,q} = \left[\left(\mathbf{H}_j^{(k_{q,1})}\right)^T, \left(\mathbf{H}_j^{(k_{q,1}+\mathcal{D})}\right)^T, \cdots, \left(\mathbf{H}_j^{(k_{q,2})}\right)^T\right]^T$ denote the q-th submatrix of $\mathbf{H}_j$, whose size is $L_q \times 1$, where L_q is expressed as

$$L_q = \left\lfloor\frac{2L-q-2}{\mathcal{D}}\right\rfloor + 1. \tag{50}$$

Furthermore, $\mathbf{H}_{j,q}^{(k)}$ represents the k-th row of $\mathbf{H}_{j,q}$. The (m_1+q)-th symbol flowing to the energy harvester can be expressed as

$$\begin{aligned} &y_{EH,j}^{\mathcal{D}}[m_1+q] \\ &= \sqrt{\rho_j}\sum_{k=1}^{2L-1}\sum_{n=1}^{N}\mathbf{H}_j^{(k)}\mathbf{g}_n s_n^{\mathcal{D}}[m_1+q-k+1] + \sqrt{\rho_j}z_j^{\mathcal{D}}[m_1+q] \\ &= \sqrt{\rho_j}\sum_{k=1}^{L_q}\sum_{n=1}^{N}\mathbf{H}_{j,q}^{(k)}\mathbf{g}_n s_n^{\mathcal{D}}[m_1-(k-1)\mathcal{D}] + \sqrt{\rho_j}z_j^{\mathcal{D}}[m_1+q], \end{aligned} \tag{51}$$

for $\forall q = 0, 1, \cdots, \mathcal{D}-1$. Let $m_1 = p\mathcal{D}$ for $p \in \mathbb{N}$. The average RF power $\overline{P_{EH,j}}\left(\widehat{\mathcal{G}}, \rho_j\right)$ input to the energy harvester of the j-th receiver can be expressed as Eq. (52) on the next page.

Appendix C
Average Power Expression Eq. (16) of Information Decoder.

Let us define $m_2 = m\mathcal{D}+L-1$, where m belongs to the set $\{m|0 \leq m \leq M-1, m \in \mathbb{N}\}$, the information symbol before down-sampling operation can be expressed as

$$\begin{aligned} y_{ID,j}^{\mathcal{D}}[m_2] &= \sqrt{1-\rho_j}\sum_{k=1}^{2L-1}\sum_{n=1}^{N}\mathbf{H}_j^{(k)}\mathbf{g}_n s_n^{\mathcal{D}}[m\mathcal{D}+L-k] \\ &\quad + \sqrt{1-\rho_j}z_j^{\mathcal{D}}[m_2]. \end{aligned} \tag{53}$$

Only if mod $(L-k, \mathcal{D}) = 0$, the symbol $s_j^{\mathcal{D}}[m_2]$ is non-zero. Since the row index of $\mathbf{H}_j$ satisfies $1 \leq k \leq 2L-1$, we can obtain

$$-\left\lfloor\frac{L-1}{\mathcal{D}}\right\rfloor \leq \frac{L-k}{\mathcal{D}} \leq \left\lfloor\frac{L-1}{\mathcal{D}}\right\rfloor. \tag{54}$$

Then $y_{ID,j}^{\mathcal{D}}[m_2]$ can be reformulated as

$$\begin{aligned} y_{ID,j}^{\mathcal{D}}[m_2] &= \sqrt{1-\rho_j}\sum_{p=-\left\lfloor\frac{L-1}{\mathcal{D}}\right\rfloor}^{\left\lfloor\frac{L-1}{\mathcal{D}}\right\rfloor}\sum_{n=1}^{N}\left\{\mathbf{H}_j^{(L-p\mathcal{D})}\mathbf{g}_n s_j^{\mathcal{D}}[m\mathcal{D}+p\mathcal{D}]\right\} \\ &\quad + \sqrt{1-\rho_j}z_j^{\mathcal{D}}[m_2]. \end{aligned} \tag{55}$$

Therefore, the down-sampling symbol $y_{ID,j}[m]$ is expressed as

$$\begin{aligned} y_{ID,j}[m] &= \sqrt{1-\rho_j}\sum_{p=-\left\lfloor\frac{L-1}{\mathcal{D}}\right\rfloor}^{\left\lfloor\frac{L-1}{\mathcal{D}}\right\rfloor}\sum_{n=1}^{N}\left\{\mathbf{H}_j^{(L-p\mathcal{D})}\mathbf{g}_n s_j\left[m+p-\left\lfloor\frac{L-1}{\mathcal{D}}\right\rfloor\right]\right\} \\ &\quad + \sqrt{1-\rho_j}z_j[m] + v_j[m]. \end{aligned} \tag{56}$$

The average RF power $\overline{P_{ID,j}}\left(\widehat{\mathcal{G}}, \rho_j\right)$ input to the information decoder of the j-th receiver is expressed as Eq. (57) on the next page.

Appendix D
Proof of the Convergence for Algorithm 2.

We denote the k-th iteration of the fair-throughput in the Algorithm 2 as $R_{fair}^{(k)}$, while the variables are denoted as $\widehat{\mathcal{G}}^{(k)}$, $\rho_j^{(k)}$ and $\psi_j^{ID(k)}$, respectively. Then the monotonicity of $R_{fair}^{(k)}$ with respect to k is derived as

$$\begin{aligned} R_{fair}^{(k)} &= \min_j R_j\left(\widehat{\mathcal{G}}^{(k)}, \rho_j^{(k)}\right) \\ &\overset{(a)}{=} \min_j \widetilde{R}_j\left(\widehat{\mathcal{G}}^{(k)}, \rho_j^{(k)}, \psi_j^{ID(k)}\right) \\ &\leq \min_j \widetilde{R}_j\left(\widehat{\mathcal{G}}^{(k+1)}, \rho_j^{(k)}, \psi_j^{ID(k)}\right) \\ &\leq \min_j \widetilde{R}_j\left(\widehat{\mathcal{G}}^{(k+1)}, \rho_j^{(k+1)}, \psi_j^{ID(k)}\right) \\ &\leq \min_j \widetilde{R}_j\left(\widehat{\mathcal{G}}^{(k+1)}, \rho_j^{(k+1)}, \psi_j^{ID(k+1)}\right) \\ &\overset{(b)}{=} \min_j R_j\left(\widehat{\mathcal{G}}^{(k+1)}, \rho_j^{(k+1)}\right) = R_{fair}^{(k+1)}. \end{aligned} \tag{58}$$

$$\begin{aligned}\overline{P_{EH,j}}\left(\widehat{\mathcal{G}},\rho_j\right) &= \lim_{M\to\infty}\frac{1}{M\mathcal{D}T_s}\sum_{p=0}^{M-1}\sum_{q=0}^{\mathcal{D}-1}T_s y_{EH,j}^{\mathcal{D}}\left[p\mathcal{D}+q\right]y_{EH,j}^{\mathcal{D}\dagger}\left[p\mathcal{D}+q\right] = \frac{\rho_j}{\mathcal{D}}\sum_{n=1}^{N}\sum_{q=0}^{\mathcal{D}-1}\sum_{k=1}^{L_q}\mathbf{H}_{j,q}^{(k)}\mathbf{g}_n\left\{\lim_{M\to\infty}\frac{1}{M}\sum_{p=0}^{M-1}s_n^{\mathcal{D}}\left[p\mathcal{D}-(k-1)\mathcal{D}\right]\right.\\ &\left.\cdot\, s_n^{\mathcal{D}\dagger}\left[p\mathcal{D}-(k-1)\mathcal{D}\right]\right\}\mathbf{g}_n^{\dagger}\mathbf{H}_{j,q}^{(k)\dagger} + \frac{\rho_j}{\mathcal{D}}\sum_{q=0}^{D-1}\left\{\lim_{M\to\infty}\frac{1}{M}\sum_{p=0}^{M-1}\left[z_j^{\mathcal{D}}\left[p\mathcal{D}+q\right]z_j^{\mathcal{D}\dagger}\left[p\mathcal{D}+q\right]\right]\right\}\\ &= \frac{\rho_j}{\mathcal{D}}\sum_{n=1}^{N}\sum_{q=0}^{\mathcal{D}-1}\sum_{k=1}^{L_q}\mathbf{H}_{j,q}^{(k)}\mathbf{g}_n\left\{\lim_{M\to\infty}\frac{1}{M}\sum_{p=0}^{M-1}\left[s_n\left[p-(k-1)\right]s_n^{\dagger}\left[p-(k-1)\right]\right]\right\}\mathbf{g}_n^{\dagger}\mathbf{H}_{j,q}^{(k)\dagger} + \frac{\rho_j}{\mathcal{D}}\sum_{q=0}^{D-1}\sigma_z^2\\ &= \frac{\rho_j}{\mathcal{D}}\sum_{n=1}^{N}\sum_{q=0}^{\mathcal{D}-1}\sum_{k=1}^{L_q}\mathbf{H}_{j,q}^{(k)}\mathbf{g}_n\mathbf{g}_n^{\dagger}\mathbf{H}_{j,q}^{(k)\dagger} + \rho_j\sigma_z^2 = \frac{\rho_j}{\mathcal{D}}\sum_{n=1}^{N}\sum_{k=1}^{2L-1}\mathbf{H}_j^{(k)}\mathbf{g}_n\mathbf{g}_n^{\dagger}\mathbf{H}_j^{(k)\dagger} + \rho_j\sigma_z^2. \end{aligned} \tag{52}$$

$$\begin{aligned}\overline{P_{ID,j}}\left(\widehat{\mathcal{G}},\rho_j\right) &= \lim_{M\to\infty}\frac{1}{MT_s}\sum_{m=0}^{M-1}T_s y_{ID,j}\left[m\right]y_{ID,j}^{\dagger}\left[m\right] = \left(1-\rho_j\right)\sum_{p=-\left\lfloor\frac{L-1}{\mathcal{D}}\right\rfloor}^{\left\lfloor\frac{L-1}{\mathcal{D}}\right\rfloor}\sum_{n=1}^{N}\mathbf{H}_j^{(L-p\mathcal{D})}\mathbf{g}_n\left\{\lim_{M\to\infty}\frac{1}{MT_s}\sum_{m=0}^{M-1}T_s s_j\left[m+p-\left\lfloor\frac{L-1}{\mathcal{D}}\right\rfloor\right]\right.\\ &\left.\cdot\, s_j^{\dagger}\left[m+p-\left\lfloor\frac{L-1}{\mathcal{D}}\right\rfloor\right]\right\}\mathbf{g}_n^{\dagger}\mathbf{H}_j^{(L-p\mathcal{D})\dagger} + \lim_{m\to\infty}\frac{1-\rho_j}{MT_s}\sum_{m=0}^{M-1}T_s z_j\left[m\right]z_j^{\dagger}\left[m\right] + \lim_{m\to\infty}\frac{1}{MT_s}\sum_{m=0}^{M-1}T_s v_j\left[m\right]v_j^{\dagger}\left[m\right]\\ &= \left(1-\rho_j\right)\sum_{p=-\left\lfloor\frac{L-1}{\mathcal{D}}\right\rfloor}^{\left\lfloor\frac{L-1}{\mathcal{D}}\right\rfloor}\sum_{n=1}^{N}\mathbf{H}_j^{(L-p\mathcal{D})}\mathbf{g}_n\mathbf{g}_n^{\dagger}\mathbf{H}_j^{(L-p\mathcal{D})\dagger} + \left(1-\rho_j\right)\sigma_z^2 + \sigma_{cov}^2. \end{aligned} \tag{57}$$

Note that (a) and (b) are obtained since (P1) and (P3) have the same optimal objective value when the auxiliary variable $\mathbf{\Psi}^{ID}$ is optimal. Moreover, the fair-throughput satisfies

$$\begin{aligned}R_{fair} &= \min_j\frac{B}{\mathcal{D}}\log_2\left(1+\gamma_j\left(\widehat{\mathcal{G}},\rho_j\right)\right)\\ &\overset{(c)}{\leq}\min_j\frac{B}{\mathcal{D}}\log_2\left(1+\frac{\left(1-\rho_j\right)\mathbf{H}_j^{(L)}\mathbf{g}_j\mathbf{g}_j^{\dagger}\mathbf{H}_j^{(L)\dagger}}{\sigma_{cov}^2}\right)\\ &\overset{(d)}{\leq}\min_j\frac{B}{\mathcal{D}}\log_2\left(1+\frac{\left\|\mathbf{H}_j^{(L)}\right\|_2^2\left\|\mathbf{g}_j\right\|_2^2}{\sigma_{cov}^2}\right)\\ &\overset{(e)}{<}+\infty. \end{aligned} \tag{59}$$

where (c) holds, since we remove the ISI and IRI in the denominator of the $\gamma_j\left(\widehat{\mathcal{G}},\rho_j\right)$; (d) holds due to the constraint (19d) and the Cauchy-Schwarz inequality [57]; (e) holds according to the constraints (21) and (22). Finally, $R_{fair}^{(k)}$ increases monotonously and it is upper-bounded by a finite value. Therefore, Algorithm 2 converges to a stationary point.

References

[1] Q.-V. Pham, R. Ruby, F. Fang, D. C. Nguyen, Z. Yang, M. Le, Z. Ding, and W.-J. Hwang, "Aerial computing: A new computing paradigm, applications, and challenges," *IEEE Internet of Things Journal*, vol. 9, no. 11, pp. 8339–8363, 2022.

[2] Y. Mao, O. Dizdar, B. Clerckx, R. Schober, P. Popovski, and H. V. Poor, "Rate-splitting multiple access: Fundamentals, survey, and future research trends," *IEEE Communications Surveys and Tutorials*, pp. 1–1, 2022.

[3] S. Wang, R. Han, Y. Hong, Q. Hao, M. Wen, L. Musavian, S. Mumtaz, and D. W. Kwan Ng, "Robotic wireless energy transfer in dynamic environments: System design and experimental validation," *IEEE Communications Magazine*, vol. 60, no. 3, pp. 40–46, 2022.

[4] Q. Wu, X. Guan, and R. Zhang, "Intelligent reflecting surface-aided wireless energy and information transmission: An overview," *Proceedings of the IEEE*, vol. 110, no. 1, pp. 150–170, 2022.

[5] J. Hu, Q. Wang, and K. Yang, "Energy self-sustainability in full-spectrum 6g," *IEEE Wireless Communications*, vol. 28, no. 1, pp. 104–111, 2021.

[6] Y. Zhao, J. Hu, K. Yang, and K.-K. Wong, "Unary coding design for simultaneous wireless information and power transfer with practical m-qam," *IEEE Transactions on Wireless Communications*, vol. 20, no. 5, pp. 2850–2862, 2021.

[7] M. Zhang and X. Cheng, "Spatial-modulation-based wireless-powered communication for achievable rate enhancement," *IEEE Communications Letters*, vol. 21, no. 6, pp. 1365–1368, 2017.

[8] Y. Zhao, J. Hu, A. Xie, K. Yang, and K.-K. Wong, "Receive spatial modulation aided simultaneous wireless information and power transfer with finite alphabet," *IEEE Transactions on Wireless Communications*, vol. 19, no. 12, pp. 8039–8053, 2020.

[9] Y. Zhao, Y. Wu, J. Hu, and K. Yang, "Time-index modulation for integrated data and energy transfer: A remedy for time switching," *IEEE Wireless Communications Letters*, vol. 11, no. 9, pp. 1815–1819, 2022.

[10] I. Krikidis and C. Psomas, "Tone-index multisine modulation for swipt," *IEEE Signal Processing Letters*, vol. 26, no. 8, pp. 1252–1256, 2019.

[11] Y. Zhao, Y. Wu, J. Hu, and K. Yang, "A general analysis and optimization framework of time index modulation for integrated data and energy transfer," *IEEE Transactions on Wireless Communications*, 2022.

[12] S. Yin and Z. Qu, "Resource allocation in multiuser ofdm systems with wireless information and power transfer," *IEEE Communications Letters*, vol. 20, no. 3, pp. 594–597, 2016.

[13] B. Clerckx, "Wireless information and power transfer: Nonlinearity, waveform design, and rate-energy tradeoff," *IEEE Transactions on Signal Processing*, vol. 66, no. 4, pp. 847–862, 2018.

[14] B. Clerckx, R. Zhang, R. Schober, D. W. K. Ng, D. I. Kim, and H. V. Poor, "Fundamentals of wireless information and power transfer: From rf energy harvester models to signal and system designs," *IEEE Journal on Selected Areas in Communications*, vol. 37, no. 1, pp. 4–33, 2019.

[15] B. Clerckx and J. Kim, "On the beneficial roles of fading and transmit diversity in wireless power transfer with nonlinear energy harvesting," *IEEE Transactions on Wireless Communications*, vol. 17, no. 11, pp. 7731–7743, 2018.

[16] R. Zhang and C. K. Ho, "Mimo broadcasting for simultaneous wireless information and power transfer," *IEEE Transactions on Wireless Communications*, vol. 12, no. 5, pp. 1989–2001, 2013.

[17] H. Lee, K.-J. Lee, H. Kim, and I. Lee, "Joint transceiver optimization for miso swipt systems with time switching," *IEEE Transactions on Wireless Communications*, vol. 17, no. 5, pp. 3298–3312, 2018.

[18] Q. Wu and R. Zhang, "Joint active and passive beamforming optimization for intelligent reflecting surface assisted swipt under qos constraints," *IEEE Journal on Selected Areas in Communications*, vol. 38, no. 8, pp. 1735–1748, 2020.

[19] B. Lyu, P. Ramezani, D. T. Hoang, S. Gong, Z. Yang, and A. Jamalipour, "Optimized energy and information relaying in self-sustainable irs-empowered wpcn," *IEEE Transactions on Communications*, vol. 69, no. 1, pp. 619–633, 2021.

[20] W. Yan, X. Yuan, Z.-Q. He, and X. Kuai, "Large intelligent surface aided multiuser mimo: Passive beamforming and information transfer," in *ICC 2020 - 2020 IEEE International Conference on Communications (ICC)*, 2020, pp. 1–7.

[21] Q. Yue, J. Hu, K. Yang, and K.-K. Wong, "Intelligent reflecting surface aided wireless power transfer with a dc-combining based energy receiver and practical waveforms," *IEEE Transactions on Vehicular Technology*, vol. 71, no. 9, pp. 9751–9764, 2022.

[22] F. Han and K. J. R. Liu, "A multiuser trdma uplink system with 2d parallel interference cancellation," *IEEE Transactions on Communications*, vol. 62, no. 3, pp. 1011–1022, 2014.

[23] Y. Chen, Y. Xiong, D. Chen, T. Jiang, S. X. Ng, and L. Hanzo, "Hybrid precoding for wideband millimeter wave mimo systems in the face of beam squint," *IEEE Transactions on Wireless Communications*, vol. 20, no. 3, pp. 1847–1860, 2021.

[24] M. U. Zia, W. Xiang, T. Huang, and I. Haider Naqvi, "Deep learning-aided tr-uwb mimo system," *IEEE Transactions on Communications*, vol. 70, no. 10, pp. 6579–6588, 2022.

[25] Y. Chen, Y.-H. Yang, F. Han, and K. J. R. Liu, "Time-reversal wideband communications," *IEEE Signal Processing Letters*, vol. 20, no. 12, pp. 1219–1222, 2013.

[26] Y. Chen, B. Wang, Y. Han, H.-Q. Lai, Z. Safar, and K. R. Liu, "Why time reversal for future 5g wireless? [perspectives]," *IEEE Signal Processing Magazine*, vol. 33, no. 2, pp. 17–26, 2016.

[27] Y. Han, Y. Chen, B. Wang, and K. J. Ray Liu, "Enabling heterogeneous connectivity in internet of things: A time-reversal approach," *IEEE Internet of Things Journal*, vol. 3, no. 6, pp. 1036–1047, 2016.

[28] Y. Han, Y. Chen, B. Wang, and K. J. R. Liu, "Time-reversal massive multipath effect: A single-antenna "massive mimo" solution," *IEEE Transactions on Communications*, vol. 64, no. 8, pp. 3382–3394, 2016.

[29] H. Ma, B. Wang, Y. Chen, and K. J. Ray Liu, "Time-reversal tunneling effects for cloud radio access network," *IEEE Transactions on Wireless Communications*, vol. 15, no. 4, pp. 3030–3043, 2016.

[30] R. C. Daniels and R. W. Heath, "Improving on time reversal with miso precoding," in *Proceedings of the Eighth International Symposium on Wireless Personal Communications Conference*, 2005, pp. 18–22.

[31] Y.-H. Yang and K. J. Ray Liu, "Waveform design with interference pre-cancellation beyond time-reversal systems," *IEEE Transactions on Wireless Communications*, vol. 15, no. 5, pp. 3643–3654, 2016.

[32] M.-L. Ku, Y. Han, H.-Q. Lai, Y. Chen, and K. J. R. Liu, "Power waveforming: Wireless power transfer beyond time reversal," *IEEE Transactions on Signal Processing*, vol. 64, no. 22, pp. 5819–5834, 2016.

[33] M.-L. Ku and J.-W. Lai, "Joint beamforming and resource allocation for wireless-powered device-to-device communications in cellular networks," *IEEE Transactions on Wireless Communications*, vol. 16, no. 11, pp. 7290–7304, 2017.

[34] D. Tse and P. Viswanath, *Fundamentals of Wireless Communication*. Cambridge University Press, 2005.

[35] F. Han, Y.-H. Yang, B. Wang, Y. Wu, and K. J. R. Liu, "Time-reversal division multiple access over multi-path channels," *IEEE Transactions on Communications*, vol. 60, no. 7, pp. 1953–1965, 2012.

[36] A. Saleh and R. Valenzuela, "A statistical model for indoor multipath propagation," *IEEE Journal on Selected Areas in Communications*, vol. 5, no. 2, pp. 128–137, 1987.

[37] B. M. Popović, "Efficient Golay correlator," *Electronics Letters*, vol. 35, no. 17, p. 1427, Jan. 1999.

[38] Z.-H. Wu, Y. Han, Y. Chen, and K. J. R. Liu, "A time-reversal paradigm for indoor positioning system," *IEEE Transactions on Vehicular Technology*, vol. 64, no. 4, pp. 1331–1339, 2015.

[39] Q. Xu, C. Jiang, Y. Han, B. Wang, and K. J. R. Liu, "Waveforming: An overview with beamforming," *IEEE Communications Surveys Tutorials*, vol. 20, no. 1, pp. 132–149, 2018.

[40] Y. Chen, F. Han, Y.-H. Yang, H. Ma, Y. Han, C. Jiang, H.-Q. Lai, D. Claffey, Z. Safar, and K. J. R. Liu, "Time-reversal wireless paradigm for green internet of things: An overview," *IEEE Internet of Things Journal*, vol. 1, no. 1, pp. 81–98, 2014.

[41] G. Kwon, H. Park, and M. Z. Win, "Joint beamforming and power splitting for wideband millimeter wave swipt systems," *IEEE Journal of Selected Topics in Signal Processing*, vol. 15, no. 5, pp. 1211–1227, 2021.

[42] X. Peng, P. Wu, H. Tan, and M. Xia, "Optimization for irs-assisted mimo-ofdm swipt system with nonlinear eh model," *IEEE Internet of Things Journal*, vol. 9, no. 24, pp. 25 253–25 268, 2022.

[43] A. Riaz, S. Zakir, M. M. Farooq, M. Awais, and W. T. Khan, "A triband rectifier toward millimeter-wave frequencies for energy harvesting and wireless power-transfer applications," *IEEE Microwave and Wireless Components Letters*, vol. 31, no. 2, pp. 192–195, 2021.

[44] R. Jiang, K. Xiong, P. Fan, Y. Zhang, and Z. Zhong, "Optimal design of swipt systems with multiple heterogeneous users under non-linear energy harvesting model," *IEEE Access*, vol. 5, pp. 11 479–11 489, 2017.

[45] E. Boshkovska, D. W. K. Ng, N. Zlatanov, and R. Schober, "Practical non-linear energy harvesting model and resource allocation for swipt systems," *IEEE Communications Letters*, vol. 19, no. 12, pp. 2082–2085, 2015.

[46] Q. Yue, J. Hu, K. Yang, and C. Huang, "Transceiver design for simultaneous wireless information and power multicast in multi-user mmwave mimo system," *IEEE Transactions on Vehicular Technology*, vol. 69, no. 10, pp. 11 394–11 407, 2020.

[47] B. Clerckx, R. Zhang, R. Schober, D. W. K. Ng, D. I. Kim, and H. V. Poor, "Fundamentals of wireless information and power transfer: From rf energy harvester models to signal and system designs," *IEEE Journal on Selected Areas in Communications*, vol. 37, no. 1, pp. 4–33, 2019.

[48] L. Liu, R. Zhang, and K.-C. Chua, "Wireless information and power transfer: A dynamic power splitting approach," *IEEE Transactions on Communications*, vol. 61, no. 9, pp. 3990–4001, 2013.

[49] K. Shen and W. Yu, "Fractional programming for communication systems—part i: Power control and beamforming," *IEEE Transactions on Signal Processing*, vol. 66, no. 10, pp. 2616–2630, 2018.

[50] G. Zhang, Q. Wu, M. Cui, and R. Zhang, "Securing uav communications via joint trajectory and power control," *IEEE Transactions on Wireless Communications*, vol. 18, no. 2, pp. 1376–1389, 2019.

[51] V. Sreedharan, "ϵ-subgradient projection algorithm," *Journal of Approximation Theory*, vol. 51, no. 1, pp. 27–46, 1987. [Online]. Available: https://www.sciencedirect.com/science/article/pii/002190458790092X

[52] Z. Wang, J. Hu, K. Yang, and J. Shen, "Link-level wideband signal shaping for downlink wireless information and energy provision," *IEEE Transactions on Vehicular Technology*, vol. 71, no. 3, pp. 3338–3343, 2022.

[53] Z. Wang, J. Hu, and K. Yang, "Siso-ofdm and miso-ofdm counterparts for "wideband waveforming for integrated data and energy transfer: Creating extra gain beyond multiple antennas and multiple carriers"," 2022. [Online]. Available: https://arxiv.org/abs/2212.04349

[54] K. Shen and W. Yu, "Fractional programming for communication systems—part ii: Uplink scheduling via matching," *IEEE Transactions on Signal Processing*, vol. 66, no. 10, pp. 2631–2644, 2018.

[55] H. Kim, H. Lee, M. Ahn, H.-B. Kong, and I. Lee, "Joint subcarrier and power allocation methods in full duplex wireless powered communication networks for ofdm systems," *IEEE Transactions on Wireless Communications*, vol. 15, no. 7, pp. 4745–4753, 2016.

[56] R. Deng, B. Di, H. Zhang, Y. Tan, and L. Song, "Reconfigurable holographic surface: Holographic beamforming for metasurface-aided wireless communications," *IEEE Transactions on Vehicular Technology*, vol. 70, no. 6, pp. 6255–6259, 2021.

[57] G. H. Golub and C. F. Van Loan, *Matrix Computations (4rd Ed.)*. USA: Johns Hopkins University Press, 2013.

Zhonglun Wang (Student Member, IEEE) received the B.Sc. degree from Jilin University, Changchun, China, in 2020. He is currently pursuing the Ph.D. degree in the School of Information and Communication Engineering, University of Electronic Science and Technology of China, Chengdu, China. His current research interests include simultaneous wireless information and power transfer, signal processing and optimization.

Jie Hu [S'11, M'16, SM' 21] (hujie@uestc.edu.cn) received his B.Eng. and M.Sc. degrees from Beijing University of Posts and Telecommunications, China, in 2008 and 2011, respectively, and received the Ph.D. degree from the School of Electronics and Computer Science, University of Southampton, U.K., in 2015. Since March 2016, he has been working with the School of Information and Communication Engineering, University of Electronic Science and Technology of China (UESTC). He is now a Research Professor and PhD supervisor. He won UESTC's Academic Young Talent Award in 2019. Now he is supported by the "100 Talents" program of UESTC. He is an editor for *IEEE Wireless Communications Letters*, *IEEE/CIC China Communications* and *IET Smart Cities*. He serves for *IEEE Communications Magazine*, *Frontiers in Communications and Networks* as well as *ZTE communications* as a guest editor. He is a technical committee member of ZTE Technology. He is a program vice-chair for IEEE TrustCom 2020, a technical program committee (TPC) chair for IEEE UCET 2021 and a program vice-chair for UbiSec 2022. He also serves as a TPC member for several prestigious IEEE conferences, such as IEEE Globecom/ICC/WCSP and etc. He has won the best paper award of IEEE SustainCom 2020 and the best paper award of IEEE MMTC 2021. His current research focuses on wireless communications and resource management for B5G/6G, wireless information and power transfer as well as integrated communication, computing and sensing.

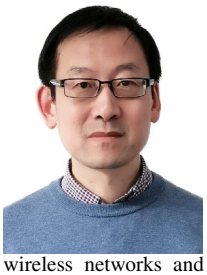

Kun Yang [M'00, SM'10, F'23] received his PhD from the Department of Electronic & Electrical Engineering of University College London (UCL), UK. He is currently a Chair Professor in the School of Computer Science & Electronic Engineering, University of Essex, leading the Network Convergence Laboratory (NCL), UK. He is also an affiliated professor at UESTC, China. Before joining in the University of Essex at 2003, he worked at UCL on several European Union (EU) research projects for several years. His main research interests include wireless networks and communications, IoT networking, data and energy integrated networks and mobile computing. He manages research projects funded by various sources such as UK EPSRC, EU FP7/H2020 and industries. He has published 400+ papers and filed 30 patents. He serves on the editorial boards of both IEEE (e.g., IEEE TNSE, IEEE ComMag, IEEE WCL) and non-IEEE journals (e.g., Deputy EiC of IET Smart Cities). He was an IEEE ComSoc Distinguished Lecturer (2020-2021). He is a Member of Academia Europaea (MAE), a Fellow of IEEE, a Fellow of IET and a Distinguished Member of ACM.

Kai-Kit Wong [M'01, SM'08, F'16] received the BEng, the MPhil, and the PhD degrees, all in Electrical and Electronic Engineering, from the Hong Kong University of Science and Technology, Hong Kong, in 1996, 1998, and 2001, respectively. After graduation, he took up academic and research positions at the University of Hong Kong, Lucent Technologies, Bell-Labs, Holmdel, the Smart Antennas Research Group of Stanford University, and the University of Hull, UK. He is Chair in Wireless Communications at the Department of Electronic and Electrical Engineering, University College London, UK. His current research centers around 5G and beyond mobile communications. He is a corecipient of the 2013 IEEE Signal Processing Letters Best Paper Award and the 2000 IEEE VTS Japan Chapter Award at the IEEE Vehicular Technology Conference in Japan in 2000, and a few other international best paper awards. He is Fellow of IEEE and IET and is also on the editorial board of several international journals. He is the Editor-in-Chief for IEEE Wireless Communications Letters since 2020.